Louisiana Tech University
Louisiana Tech Digital Commons

Doctoral Dissertations | Graduate School

Summer 8-2022

A COMPARATIVE STUDY OF MONO-STABLE AND BI-STABLE MAGNETIC SPRING BASED ENERGY HARVESTERS

Hieu Tri Nguyen
Louisiana Tech University

Follow this and additional works at: https://digitalcommons.latech.edu/dissertations

Recommended Citation
Nguyen, Hieu Tri, "" (2022). *Dissertation*. 972.
https://digitalcommons.latech.edu/dissertations/972

This Dissertation is brought to you for free and open access by the Graduate School at Louisiana Tech Digital Commons. It has been accepted for inclusion in Doctoral Dissertations by an authorized administrator of Louisiana Tech Digital Commons. For more information, please contact digitalcommons@latech.edu.

A COMPARATIVE STUDY OF MONO-STABLE AND BI-STABLE MAGNETIC SPRING BASED ENERGY HARVESTER

by

Hieu Tri Nguyen, M. S.

A Dissertation Presented in Partial Fulfillment
of the Requirements of the Degree
Doctor of Philosophy

COLLEGE OF ENGINEERING AND SCIENCE
LOUISIANA TECH UNIVERSITY

August 2022

LOUISIANA TECH UNIVERSITY

GRADUATE SCHOOL

July 20, 2022
Date of dissertation defense

We hereby recommend that the dissertation prepared by

Hieu Tri Nguyen, M. S.

entitled **A COMPARATIVE STUDY OF MONO-STABLE AND BI-STABLE MAGNETIC SPRING BASED ENERGY HARVESTERS**

be accepted in partial fulfillment of the requirements for the degree of

Doctor of Philosophy in Engineering, Materials & Infrastructure Systems Conc.

Hamzeh Bardaweel
Supervisor of Dissertation Research

Jay Xingran Wang
Head of Engineering

Doctoral Committee Members:
Hamzeh Bardaweel
Kelly Crittenden
Dentcho Genov
Leland Weiss
Sandra Zivanovic

Approved:

Hisham Hegab
Dean of Engineering & Science

Approved:

Ramu Ramachandran
Dean of the Graduate School

GS Form 13a
(01/20)

ABSTRACT

Continuous advancements in electronics manufacturing have resulted in the widespread use of low-power sensors, necessitating the development of energy harvesters capable of generating electric power from abundant and free energy sources such as ambient vibrations. A rising interest in energy harvesting technology inspires the work discussed herein using magnetic interactions to target nonlinear energy harvesting, which is compatible with ambient vibration energy sources with a broad frequency spectrum and particularly rich in low frequencies. This research aimed to look into a magnetic-levitation-based vibration energy harvester that could be tuned from a mono-stable to a bi-stable configuration. An oscillating magnet is levitated between two stationary top and bottom magnets in a mono-stable arrangement. A bi-stable configuration is achieved by fixing a cluster of peripheral solid magnets around the harvester housing. Magnetic forces in magnetic-levitation-based harvesters have traditionally been represented by polynomial functions integrated into the equation of motion. Analytical models for the interaction of magnets were developed and integrated into the equation of motion in this study. The analytical model of magnetic force delivers more accurate results for the bi-stable configuration than those produced using polynomial functions, according to the findings from this study. The results demonstrated that adjusting the geometric ratios of the peripheral magnets in the bi-stable configuration can produce a variety of load-deflection properties. The bi-stable design exhibits inter-well, chaotic, and intra-well

motion at varying accelerations during dynamic operation. The bi-stable architecture benefits from thinner peripheral magnets, especially at lower acceleration values. Lower energy barriers, improved frequency responses, and nearly zero stiffness at equilibrium position are all advantages of thinner peripheral magnets. The harvester moved towards mono-stability when thinner peripheral magnets were utilized, showing that mono-stability is the preferred mode for vibration energy harvesting under harmonic excitation. We also propose an experimental and theoretical platform for developing design platform and performing analysis on mono-stable magnetic springs used in vibration energy harvesting devices. The results reveal a high level of agreement between the model and the experiment. For linear and nonlinear stiffness coefficients, approximate analytical expressions are found. The findings indicate that the linear and nonlinear stiffness coefficients are linked. The stationary ring magnet's outer diameter can be utilized to modify the energy harvesting system's nonlinearity to provide linear, hardening nonlinear, or softening nonlinear responses. Designers can use this work to understand the behavior of magnetic spring-based harvesting systems and assess their performance concerning design factors. Other energy systems that use magnetic springs, such as energy sinks, could benefit from this research.

APPROVAL FOR SCHOLARLY DISSEMINATION

The author grants to the Prescott Memorial Library of Louisiana Tech University the right to reproduce, by appropriate methods, upon request, any or all portions of this Dissertation. It is understood that "proper request" consists of the agreement, on the part of the requesting party, that said reproduction is for his personal use and that subsequent reproduction will not occur without written approval of the author of this Dissertation. Further, any portions of the Dissertation used in books, papers, and other works must be appropriately referenced to this Dissertation.

Finally, the author of this Dissertation reserves the right to publish freely, in the literature, at any time, any or all portions of this Dissertation.

Author _____

Date _____

TABLE OF CONTENTS

ABSTRACT iii

APPROVAL FOR SCHOLARLY DISSEMINATION v

LIST OF FIGURES viii

LIST OF TABLES xii

ACKNOWLEDGMENTS xiii

CHAPTER 1 INTRODUCTION 1

1.1 Motivation 1

1.2 Objectives 3

CHAPTER 2 LITERATURE REVIEW 6

2.1 Monostable 6

2.2 Bistable 11

CHAPTER 3 DESIGN AND THEORY 13

3.1 Design 13

3.2 Theory 16

3.2.1 Dynamic Model 16

3.2.2 Magnet Interaction 17

3.2.3 Small Displacement Approximation 25

3.2.4 Open Circuit Voltage 26

3.2.5 Magnetic Damping 28

3.2.6 Electrical Power 29

CHAPTER 4 FABRICATION AND EXPERIMENT 30

4.1 Fabrication 30

4.2 Experimental Setup 34

4.2.1 Magnetic Force 34

4.2.2 Dynamic Characterization 36

CHAPTER 5 RESULTS AND DISCUSSION 40

5.1 Monostable Vs. Bistable 41

5.1.1 Model Validation 41

Magnetic Force and Potential Energy Wells 41

Open Circuit Voltage and Frequency Response 44

Phase Portrait Diagram for bistable magnetic spring 48

Power Generation 53

5.1.2 Model Simulation and Effect of Design of Bi-stability 58

5.2 Design of Magnetic Spring 64

5.2.1 Design Criteria for Stiffness Nonlinearity 64

5.2.2 Magnetic Damping 66

5.2.3 Power Generation 70

CHAPTER 6 CONCLUSIONS 78

6.1 Monostable Vs. Bistable 78

6.2 Design of Magnetic Springs 80

APPENDIX 84

BIBLIOGRAPHY 87

LIST OF FIGURES

Figure 2-1: A representative sketch of a traditional design of the mono-stable vibration energy harvester..... 7

Figure 2-2: A representative sketch of a traditional design of the bi-stable vibration energy harvester. 12

Figure 3-1: Three-dimensional representative schematic of the magnetic-spring-based vibration energy harvester design (bi-stable configuration). 15

Figure 3-2: Arrangement of magnets inside the bi-stable vibration energy harvester configuration. 17

Figure 4-1: All components of the energy harvester fabricated drawn with the SolidWorks software containing: (a) Top-magnet holder, (b) Bottom-magnet holder, (c) Core, (d) Peripheral-magnet cap, (e) Peripheral-magnet holder, (f, g, h) Base..... 33

Figure 4-2: The (a) mono-stable and the (b) bi-stable configurations of the energy harvester; the base is not presented. The peripheral-magnet cap can be seen in the bi-stable configuration..... 34

Figure 4-3: Diagram of the experimental setup used to measure nonlinear magnetic restoring forces of the levitated magnet. 36

Figure 4-4: An image of the experimental setup used to measure nonlinear magnetic restoring forces of the levitated magnet. 36

Figure 4-5: Diagram of the experimental setup used for dynamic characterization of the fabricated energy harvester. 38

Figure 4-6: An image of the experimental setup used for dynamic characterization of the fabricated energy harvester. 39

Figure 5-1: The diagrams of a) the magnetic restoring forces in the mono-stable configuration measured experimentally and obtained using models and b) the magnetic restoring forces in the bi-stable configuration measured experimentally and obtained using models..... 42

Figure 5-2: The diagrams of a) the potential-energy wells and barriers of the fabricated energy harvesters in the mono-stable configuration measured experimentally and obtained using models, and b) the potential-energy wells and barriers of the fabricated energy harvester in the bi-stable configuration measured experimentally and obtained using models. 44

Figure 5-3: Open-circuit voltage envelope of the mono-stable configuration obtained at $1.25\ \mathrm{g\ m\ s^{-2}}$ a) Forward experiment b) Backward experiment, c) Forward model, d) Backward model, e) Forward, using polynomial fit, and f) Backward, using polynomial fit. 46

Figure 5-4: Open-circuit voltage envelop of the bi-stable configuration obtained at $2.5\ \mathrm{g\ m\ s^{-2}}$ a) Forward experiment b) Backward experiment, c) Forward model, d) Backward model, e) Forward, using polynomial fit, f) Backward, using polynomial fit. 48

Figure 5-5: Phase portrait of the bi-stable energy harvester obtained at $2.5\ \mathrm{g\ m\ s^{-2}}$ a) Experiment and b) model at 15.0-15.5 Hz; c) Experiment and d) Model at 21.0-21.5 Hz, e) Experiment and f) Model at 22.5-23.0 Hz; g) Experiment and h) Model at 23.8-24.3 Hz; i) Experiment and j) Model at 35.0-35.5 Hz. 50

Figure 5-6: Displacement history of the bi-stable energy harvester obtained at $2.5\ \mathrm{g\ m\ s^{-2}}$ from experimental data. 52

Figure 5-7: Displacement history of the bi-stable energy harvester obtained at $2.5\ \mathrm{g\ m\ s^{-2}}$ from model prediction. 52

Figure 5-8: Inter-well motion obtained using model prediction at $4.0\ \mathrm{g\ m\ s^{-2}}$. 52

Figure 5-9: Power densities obtained using experiment and model simulation of the mono-stable configuration at $1.25\ \mathrm{g\ m\ s^{-2}}$. 54

Figure 5-10: Power densities obtained using experiment and model simulation of the bi-stable configuration at $2.5\ \mathrm{g\ m\ s^{-2}}$. 54

Figure 5-11. Representative examples of model simulation and measured output voltage of the mono-stable and bi-stable energy harvester configurations when connected to load resistance; $Rload$ obtained at $1.25\ \mathrm{g\ m\ s^{-2}}$ for mono-stable and $2.5\ \mathrm{g\ m\ s^{-2}}$ for bi-stable configuration: (a) Experiment at $Rload$ =100 Ω, (b) Experiment at $Rload$ =1 kΩ, (c) Experiment at $Rload$ =10 kΩ, (d) Model simulations $Rload$ =100 Ω, (e) Model simulations $Rload$ =1 kΩ, and (f) Model simulations $Rload$ =10 kΩ. 57

Figure 5-12. Peak power versus load resistance obtained using experiment and model simulation of the a) mono-stable configuration at $1.25\ \mathrm{g\ m\ s^{-2}}$ and b) bi-stable configuration at $2.5\ \mathrm{g\ m\ s^{-2}}$. 58

Figure 5-13: Model simulations of the force-displacement curves of the bi-stable energy harvester obtained for different geometric ratios of the peripheral magnets. 60

Figure 5-14: Model simulations of the potential-energy wells and barriers of the bi-stable energy harvester obtained for different geometric ratios of the peripheral magnets. 60

Figure 5-15: Comparison of open-circuit voltage envelop of the bi-stable harvester obtained for 1/32 inch (BLUE) and 1/128 inch (ORANGE) thick peripheral magnets configurations: a) Forward and b) Backward at 1 g m s − 2; c) Forward and d) Backward at 3 g (m s − 2); e) Forward and f) Backward at 5 g (m s − 2)..... 63

Figure 5-16: Design of linear and nonlinear stiffness coefficients, k1 and k3, respectively, with respect to a) volume of the levitated magnet, b) height of the stationary ring magnets, c) inner diameter of the stationary ring magnets, d) outer diameter of the stationary ring magnets, and e) distance between two stationary ring magnets. In the figure, the black circular dot and the red square dot represent the nominal values of k1 and k3, respectively, given in the nomenclature table. The solid black line and the dotted red line represent the behavior of k1 and k3, respectively, as each parameter changes. 66

Figure 5-17: Magnetic damping coefficient with respect to displacement, z, obtained using the nominal design parameters given in the nomenclature table. Simulations are performed for acceleration level 1.25 g [m/s^2], load resistance Rl = 10 kΩ, and cm = 5.5 × 10 − 3 kg/s..... 67

Figure 5-18: Close-circuit voltage frequency response obtained using model simulations at 1.25 g (m s2) across load resistors, R_l: (a) 100 Ω, (b) 1 kΩ , and (c) 10 kΩ. All model simulations are obtained using analytical force model (**Eq. 3-14**) in the equation of motion. However, $Model_{MA}$ uses analytical magnetic damping model (**Eq. 3-29**) in the equation of motion (**Eq. 3-1**), and $Model_{MS}$ uses the simplified magnetic damping model (**Eq. 3-30**) in the equation of motion (**Eq. 3-1**)..... 68

Figure 5-19: Magnetic damping coefficient, C(z), with respect to the displacement, z, and the a) effect of coil length, L , b) effect of coil diameter, d , and c) effect of coil position, ζ . The load resistance in this simulation is10 kΩ..... 70

Figure 5-20: Effect of levitated magnet volume, V, on output power obtained using model simulations across various load resistors: a) Rload = 100 Ω, b) 1,000 Ω, and c) 10,000 Ω..... 71

Figure 5-21: Effect of remnant magnetic flux density of the levitated magnet, Brf, lev, on output power obtained using model simulations across various load resistors: a) Rload = 100 Ω, b) 1,000 Ω, and c) 10,000 Ω..... 72

Figure 5-22: Effect of height of stationary magnets, (h), on output power obtained using model simulations across various load resistors: a) Rl $= 100\ \Omega$, b) $1{,}000\ \Omega$, and c) $10{,}000\ \Omega$. 72

Figure 5-23: Effect of inner diameter of stationary magnets, (a), on output power obtained using model simulations across various load resistors: a) Rload $= 100\ \Omega$, b) $1{,}000\ \Omega$, and c) $10{,}000\ \Omega$. 73

Figure 5-24: Effect of outer diameter of stationary magnets, (b), on output power obtained using model simulations across various load resistors: a) Rload $= 100\ \Omega$, b) $1{,}000\ \Omega$, and c) $10{,}000\ \Omega$. 73

Figure 5-25: Effect of distance between the two stationary magnets, (H), on output power obtained using model simulations across various load resistors: a) Rload $=$ $100\ \Omega$, b) $1{,}000\ \Omega$, and c) $10{,}000\ \Omega$. 74

LIST OF TABLES

Table 4-1: Geometric and material properties of the fabricated harvester..... 31

ACKNOWLEDGMENTS

I would like to thank Dr. Hamzeh Bardaweel for making my dissertation possible since he had helped guide the direction of my project from the very beginning of my program. I also want to thank my lab mates Ghufran Aldawood, Winner Anigbogu, and Alexander Isiani for their friendship and their constant support of my goals. I want to thank Dr. Dentcho Genov for his generosity in providing me the necessary theoretical background and being one of my committee members. Finally, I want to extend my thanks to Dr. Leland Weiss, Dr. Sandra Zivanovic, and Dr. Kelly Crittenden for kindly accepting my invitation to be in my committee.

CHAPTER 1

INTRODUCTION

This chapter discusses the motivation and the objectives of this dissertation. **Section 1.1** discusses the reasons for our work in mono-stable and bi-stable magnetic-spring based vibrational energy harvester. **Section 1.1** we point out current environmental challenges, recent development in electronics, and how our work builds upon this development to solve some of the mentioned challenges. In **Section 1.2**, we discuss the goals we want to achieve in this dissertation. Our work contains the derivation of many mathematical models that simulate the behavior of our devices, the design and fabrication process of the devices, models validation through experimental tests performed on our device, characterization, and parametric study.

1.1 Motivation

Low-power sensors for wireless networks and portable gadgets [1], [2], medical implants [3]–[7], and data transmission have all been used as a result of continuous improvements in electronics manufacturing [8]. The development of energy harvesters capable of generating electric power utilizing abundant and free-energy sources such as ambient vibrations has become important due to technological advancements [9]. Energy harvesting from ambient vibrations has the potential to lead to the development of small, maintenance-free, stand-alone power sources with high power density. Ambient vibrations have a power density of about 500 W cm^{-3} in most cases [10]. Ambient

vibrations are an ideal power source candidate for low-power sensors found in Wireless Sensor Networks (WSN) and portable electronics because of their high-power density. Continuous or semi-continuous oscillations with a wide range of frequencies caused by structures such as highway bridges are examples of ambient vibrations.

On energy harvesting techniques and methodologies, there is a substantial body of literature and study [11], [12]. Wearable smart electronics and gadgets [13], implantable devices [6], health monitoring devices, and wireless sensor network systems are all examples of rapidly emerging technologies. These new technologies are gaining popularity because they are light and portable [14], and they have the potential to improve the lives of millions of people throughout the world. In addition, the Internet of Things (IoT) is predicted to revolutionize the world in the near future by connecting billions of devices. The IOT will lead to interactive settings with WSN that can communicate information. As a result, these sensors will be able to collect and transmit real-time data about their surroundings, such as temperature, pressure, gas leaks, humidity, and so on. This would open up worldwide economic opportunities and solve challenges relating to pressing global requirements such as energy, water, food scarcity, greenhouse gas emissions, and terrorism.

The majority of today's portable electronics and smart devices, as well as other emerging sensing technologies, are powered by traditional techniques, such as chemical batteries. Because of the constant need for replacement and maintenance [13] as well as repetitive charging [15], the usage of these conventional chemical batteries poses a significant challenge. Furthermore, conventional chemical batteries are unsuitable for usage due to their short lifespan, dangerous disposal, and negative environmental impact

[16]. The hazardous chemicals and metals contained in these chemical batteries have a terrible environmental impact, posing a severe threat to human health and the environment [17].

The ensuing discussion demonstrates that there is a pressing global need for alternative-energy, environmentally friendly, and clean solutions to power these gadgets [18]. In this regard, the European Union (EU) has set aims to reduce traditional non-renewable energy sources by over 90% in the next 30 years [19]. The growing requirement for unconventional power sources has generated interest in exploiting freely and abundantly available energy sources from the surrounding environment to provide essential electric power to operate these gadgets. Furthermore, continuing advances in electronics manufacturing have resulted in a new class of sensors with low power consumption [2]. These characteristics have paved the way for international research efforts to develop energy harvesting systems that use accessible energy sources to generate the electric power required to run these low-power sensors and devices.

1.2 Objectives

The current research centered on creating theoretical models and conducting experiments to directly compare the mono-stable energy harvester architecture to its bi-stable counterpart. For example, forces due to magnetic contact, potential-energy wells, voltage response, inter-well, intra-well, chaotic regimes, and power metrics are all examined in this thesis. Analytical models explaining the interaction of magnets in both mono-stable and bi-stable configurations were also constructed as part of the current research. The created force models were then integrated into the harvester's equation of motion to understand the system's dynamic behavior better. The research described here

created precise models for both mono-stable and bi-stable vibration energy harvesting systems. The impact of these peripheral magnets on the harvester's performance was explored in this study since the cluster of magnets is an important design component in the bi-stable design.

Our focus then shifts to the experimental and theoretical investigation of design aspects and analysis of nonlinear magnetic springs, which are increasingly being used in vibration energy harvesting systems, as shown in **Fig. 1**, in order to assist designers in understanding and investigating the dynamic response of the energy harvester and its performance in light of its design parameters, such as geometry, dimensions, and material properties. The current research focuses on design recommendations and rules for stiffness nonlinearity and damping obtained from magnetic springs, which are frequently employed in vibration energy harvesting systems.

First, analytical models of the nonlinear magnetic force and magnetic damping force are described in this paper. Second, magnetic force and magnetic damping formulations are directly implemented into the energy harvester's equation of motion, allowing designers to explicitly understand and investigate the harvester's dynamic response and performance in light of its design parameters, which include geometry, dimensions, and material properties.

The Runge-Kutta method is used to solve the harvesting system's equation of motion, which is formulated using the derived analytical formulas for both magnetic force and magnetic damping. The results of simulations are compared to experimental data in this study. This work also makes a significant addition by obtaining approximate analytical formulations for equivalent linear and nonlinear stiffness coefficients, i.e., k_1

and k_3, respectively. In addition, the corresponding magnetic damping coefficient, c_m, is calculated, and the simplified expression's correctness is assessed. In the current study, the design elements of the magnetic spring-based vibration energy harvester are explored, as well as the analysis of various design parameters.

This dissertation incorporates work from four publications by the author, previously published in November 2018 [20], November 2019 [21], February 2020 [22], and April 2020 [23]. It is reproduced here with the permission from all the coauthors involved in this study. Chapter 2 reviews the literature about mono-stable and bi-stable vibrational energy harvesters. Chapter 3 discusses the design of our energy harvester and the theory of the working mechanism of the device. Chapter 4 addresses the fabrication process of the device and the experiments that have been carried out to verify our models and characterize the device. Chapter 5 discusses the results that we observed from the theory and experiment and our discussion about the results. Finally, Chapter 6 goes over the conclusions we made based on our observation of the theory and experimental results.

CHAPTER 2

LITERATURE REVIEW

This chapter is about the work that has been done by other researchers with regards to mono-stability and bi-stability in magnetic spring based vibrational energy harvester. **Section 2.1** focuses on mono-stability, while **Section 2.2** focuses on bi-stability. **Section 2.1** discusses a generic design of a mono-stable vibrational energy harvester and past attempts to mathematically model the behavior of this design. **Section 2.2** discusses the typical design of a bi-stable vibrational energy harvester and illustrates how bi-stability is different from mono-stability. **Section 2.3** revisits mono-stability with a focus on parametric study. **Section 2.3** shows past attempts to understand the mono-stable energy harvester's behavior and approximate the behavior through simplified models. **Section 2.3** points out the gap in our understanding of mono-stability and we discuss how our work can fill in the gap and be used for design guidelines of mono-stable energy harvesters. This chapter incorporates work from four publications by the author, previously published in November 2018 [20], November 2019 [21], February 2020 [22], and April 2020 [23]. It is reproduced here with the permission from all the coauthors involved in this study.

2.1 Monostable

Figure 2-1 shows a mono-stable magnetic-spring-based energy harvester as an example. The mono-stable harvester is made up of two (or more) magnets placed in a

repulsive arrangement, with like-poles facing each other [24]–[28]. Between the levitated magnet and the fixed magnets, this combination produces a repulsive nonlinear restoring force. This results in a mono-stable behavior with a single-well potential-energy function and one stability point of the levitated magnet. Duffing's equation can be used to describe the mono-stable magnetic-spring-based energy harvester [27], [29]. When compared to a linear energy harvester, such systems are known to exhibit bifurcations in the amplitude of the induced oscillations and may manifest a larger frequency response for a given set of parameters.

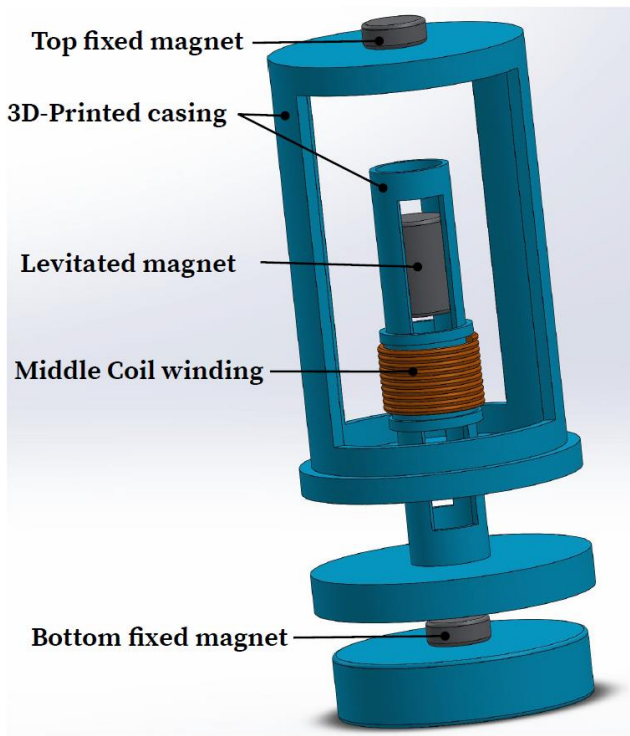

Figure 2-1: A representative sketch of a traditional design of the mono-stable vibration energy harvester.

A number of studies have been conducted to better understand the behavior of mono-stable magnetic-levitation-based nonlinear energy harvesting systems [24], [27],

[29]. Mann *et al*. suggested a mono-stable nonlinear magnetic-levitation-based energy harvester with a hardening response to increase the frequency bandwidth [27]. Based on the nonlinear restoring force of a magnetic spring, a nonlinear mathematical model of the energy harvester was built. The model revealed unique characteristics of this nonlinear energy harvester. For example, in response to harmonic excitations, the energy harvester has periodic solutions in its vibration. It also revealed the saddle-node point phenomenon, which is a rare frequency jump phenomenon [30], [31]. A series of trials were compared to models from the literature, and the theoretical response of the energy harvester was comparable.

Apo *et al*. demonstrated a mono-stable magnetic-levitation-based energy harvester with twofold repulsion [24]. The force field, magnetic flux, and dynamic response of the harvester were studied using a mathematical, nonlinear spring-mass-damper model. The model was then utilized to create an AA-sized energy harvester based on magnetic levitation. To keep a displacement rod from flipping and realigning itself, the harvester employed ring magnets around it. At 1 g acceleration and 16 Hz, the harvester produced 12.9 mW. Berdy *et al*., meanwhile, developed a mono-stable energy harvester based on magnetic levitation of block-shaped magnets rather than cylindrical magnets, allowing for thinner devices [25]. A guide rail was employed to orient the levitated magnet and prevent it from flipping and realigning itself on the manufactured harvester. At 6.7 Hz, the energy harvester produced 410 W and 0.1 g. The energy harvester's nonlinear magnetic restoring force and flux were modeled and fed into a lumped-parameter nonlinear-spring-mass damper model. Dry friction was also included

in the model as a source of energy dissipation within the energy harvester. The model's results were comparable to experimental data.

A magnetic-levitation-based energy harvester was also studied theoretically and experimentally by Marco Santo *et al*. [26]. The dynamic behavior of the mono-stable energy harvester was predicted using a semi-analytical nonlinear model. The magnetic field and magnetic force were calculated using current loops in the model. The Karnopp friction model was also employed to account for dry friction between the levitated magnet and the casing walls. Experimental data was compared to both the transient and steady-state solutions, and both revealed less than 15% inaccuracy. Lee *et al*. [29] used a model and an experiment to study a three-magnet levitation-based energy harvester. The magnetic force-displacement connection was fitted to a fifth order polynomial in their research. Then, based on Duffing's equation, a nonlinear equation of motion was introduced. The model's results were compared to those obtained in an experiment using random broadband vibration rather than harmonic excitation.

When the energy harvester was subjected to random wideband vibration, the output power was significantly reduced. While numerous stable solutions exist, the energy harvester has a tendency to return to the lowest energy state, according to the study. The energy harvester always reverts to the least energy state for a random broadband vibration, requiring continuous external input to sustain high energy orbits. Green *et al*. [32], [33] looked at the influence of friction in the presence of a magnetically levitated energy harvester. Different friction models were developed and investigated experimentally, including Coulomb, hyperbolic tangent, and LuGre. The Coulomb friction model produced the best fit with data from the experiment, according to Green *et.*

al.'s findings. Several more investigations came to similar conclusions and took similar approaches toward broadband nonlinear mono-stable magnetic-levitation-based energy harvesting [28], [34]–[38].

The equation of motion of the harvester was often utilized to link the two models using polynomial fitting and numerical integration. The magnetic force and flux were first calculated using finite element analysis. The acquired magnetic force was then fitted to a polynomial function and employed in the equation of motion of the system, together with average flux, which was then solved using numerical integration.

According to the state-of-the-art, a large number of previous studies have used experimental methods or a combination of experimental and modeling (numerical and analytical) techniques to describe the magnetic interactions (spring force and magnetic damping) present in magnetic-spring-based vibration energy harvesters. The magnetic force was then fitted to a polynomial function, $k_1z + k_3z$, to represent the nonlinear magnetic force, while the magnetic damping was assumed to be linearly dependent on the velocity of the moving magnet, i.e., $c_m z$, and the damping coefficient, c_m, was set to a constant value obtained through experiment or model. After that, the magnetic spring force, $k_1z + k_3z$, and magnetic damping force, $c_m z$, were incorporated into the equation of motion and solved to give the harvester's dynamic response.

While recent studies have focused on employing a combination of experimental approaches and theoretical models to examine these dynamic systems, certain features such as design guidelines for magnetic springs for vibration energy harvesting are still missing, to the best of our knowledge. As a result, the goal of this article is to provide a comprehensive understanding of the consequences of various design parameters, as well

as to establish successful design recommendations and a roadmap for magnetic spring-based vibration energy harvesting systems.

2.2 Bistable

Figure 2-2 is a cartoon schematic of a classic bi-stable magnetic levitation-based energy harvester. Bi-stable and multi-stable energy harvesters commonly use a mix of magnets and piezoelectric cantilevers, according to the literature [39]–[46]. While the piezoelectric cantilever extracts power in these harvesters, the magnetic spring provides the nonlinear restoring force required for bi-stability, as seen in **Figure 1-2**. Yang *et al*. gave a comprehensive overview of these harvesters [44]. Ferrari *et al*., for example, created a bi-stable magnetic-spring-based energy harvester employing a PZT layer formed on top of a steel cantilever and permanent magnets [41]. When compared to a linear energy harvester, the results from their energy harvester revealed a considerable improvement in output voltage and device bandwidth. By putting an extra magnet between the two fixed magnets, Lan and Qin proposed an improved bi-stable magnetic-spring based energy harvester [43]. The additional magnet reduced the potential energy barrier, thus allowing the harvester to travel more readily between the two stable positions, according to their findings [43]. Wang *et al*., on the other hand, used a mechanical spring amplifier to magnify the base excitation by supplying enough kinetic energy to break through the potential-energy barrier [40]. When compared to a normal bi-stable magnetic-spring-based energy harvester, their results indicated a bigger displacement and improved performance. Zhou, on the other hand, studied a tri-stable oscillator both theoretically and empirically [45]. The oscillator was subjected to

harmonic stimulation in the 1-20 Hz range, and its performance was compared to that of a bi-stable competitor.

In comparison to its rival bi-stable configuration, the results revealed that tri-stable arrangements can overcome possible energy barriers and are hence more ideal for efficient power generation through operation over a larger frequency spectrum. Cao *et al*. investigated potential energy barriers in tri-stable energy harvesters employing a combination of magnets and piezoelectric cantilevers using numerical and experimental methods [46]. The potential energy barriers are determined by the polynomial coefficients of the nonlinear magnetic restoring force and geometric parameters of the tri-stable energy harvester, according to their findings. Energy harvesters with higher order multi-stable stability have also been researched [47]–[49]. Zhou *et al*., for example, demonstrated a quad-stable energy harvester based on a piezoelectric bimorph cantilever and four magnets [47].

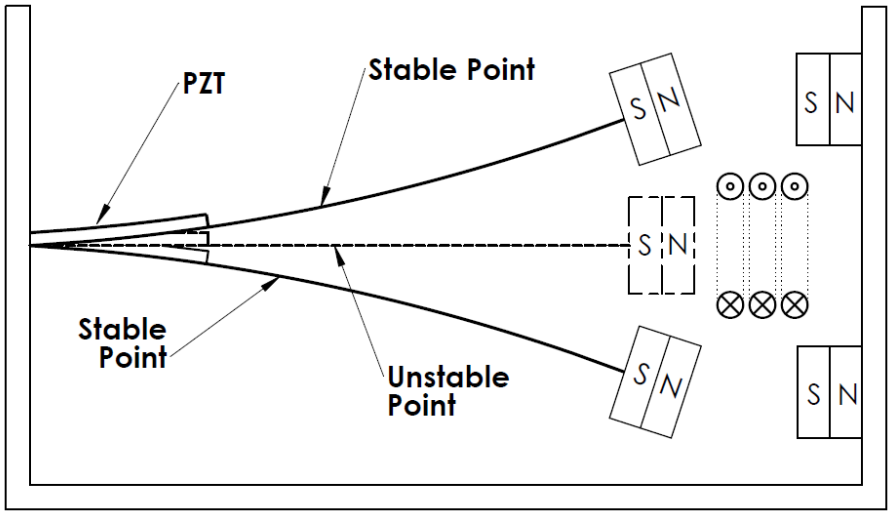

Figure 2-2: A representative sketch of a traditional design of the bi-stable vibration energy harvester.

CHAPTER 3

DESIGN AND THEORY

This chapter discusses about the schematic designs of the energy harvester in both its mono-stable mode and bi-stable mode in **Section 3.1**. The chapter also discusses the theory of the energy harvester's working mechanism in **Section 3.2**. Mathematical models are derived from first principles to describe the vibrational dynamic and electrodynamic characteristic of the energy harvester. **Section 3.2.1** and **3.2.2** discuss our approach to model the vibration dynamic of our device using first-principles. **Section 3.2.3** discusses how we approximate the vibration dynamic models developed in the previous sub-sections. **Sections 3.2.4**, **3.2.5**, and **3.2.6** discuss the derivation of electromagnetic models used to simulate the electrical output of the device. This chapter incorporates work from four publications by the author, previously published in November 2018 [20], November 2019 [21], February 2020 [22], and April 2020 [23]. It is reproduced here with the permission from all the coauthors involved in this study.

3.1 Design

An example schematic of the bi-stable configuration harvester design used in this study is shown in **Figure 3-1**. As illustrated in **Figure 3-1**, the design comprises of two fixed top and bottom ring magnets, as well as a levitated magnet surrounded by a cluster

of peripheral magnets. Mann and Owens were the first to offer a comparable design approach [50]. Mono-stable and bi-stable magnetic-interaction-based harvesters can be directly compared using the adopted idea. Because the energy harvester relies solely on magnetic interactions and does not require piezoelectric parts, it is capable of direct comparison. Because piezoelectric materials are used, there are significant variations between mono-stable and bi-stable magnetic-levitation-based energy harvesters, making direct comparison unfeasible. The inherent high internal resistance of piezoelectric is a significant disadvantage. As a result, a high load resistance, typically on the range of 60 kΩ, is necessary for optimal power transfer [40], [51]. Because of the high resistance, the output currents are very low, much below the 50 mA threshold necessary to run ordinary low-power sensors. Electromagnetic harvesters have a lower output impedance than piezoelectric harvesters. The mass of the magnet in an electromagnetic harvester reduces the harvester's resonance frequency, allowing for even more low-frequency specialization [52]. As a result, electromagnetic energy harvesters [53], [54] are arguably more suitable for real-world applications, and there are significant advantages to replacing piezoelectric elements (which are traditionally used in bi-stable vibration energy harvesters) with electromagnetic components.

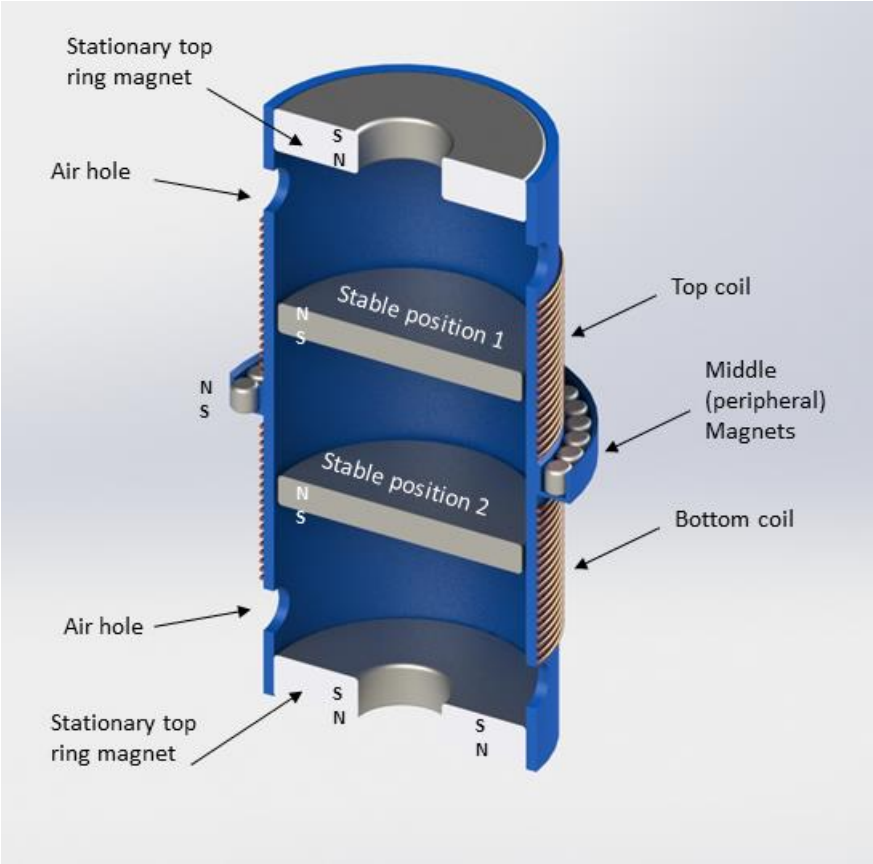

Figure 3-1: Three-dimensional representative schematic of the magnetic-spring-based vibration energy harvester design (bi-stable configuration).

While **Figure 3-1** only displays a bi-stable setup, numerous layers of middle (peripheral) magnets can be used to create a higher order multi-stable design. Nonetheless, only mono-stable and bi-stable topologies are considered in this study. For power extraction, top and bottom copper coil sections were put around the harvester's body, and air holes were created in the harvester to facilitate air flow and reduce overall damping, unlike previous bi-stable designs [39]–[46], [49], [55].

3.2 Theory

The vibration energy harvester's dynamic and static behavior, as well as the effect of crucial design parameters on the harvester's performance, were studied using a mathematical model.

3.2.1 Dynamic Model

The energy harvester shown in **Figure 3-2** was modeled as a single-degree-of-freedom mechanical system with the effective mass attached to a magnetic spring and damper. In this energy harvester, an external source of vibration causes the levitated magnet mass, m, to move vertically with absolute displacement, x. In this work, it is assumed that the lateral (radial) movement of the moving magnet is absent. The relative displacement of the levitated magnet, z, with respect to the excitation source, y, can be expressed as, $z = x - y$. The equation of motion describing the displacement of the levitated magnet mass is given by

$$m\ddot{x} - (F_{mag} + F_{damp} + F_{eddy} + F_g) = 0, \qquad \textbf{Eq. 3-1}$$

where F_{mag} is the magnetic restoring force due to the interaction between the levitated magnet and the surrounding fixed magnets, $F_{damp} = -c\dot{z} = -c(\dot{x} - \dot{y})$ is the damping force due to structural and aerodynamic energy losses, F_{eddy} is the damping force due to the induced current when the circuit is closed, and $F_g = -mg$ is the gravitational force.

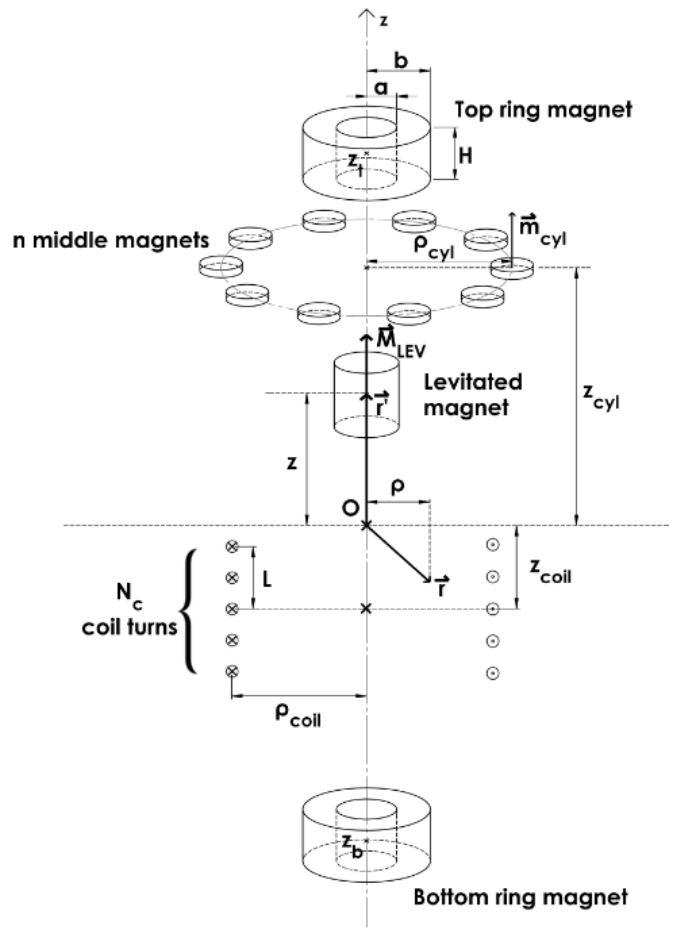

Figure 3-2: Arrangement of magnets inside the bi-stable vibration energy harvester configuration.

3.2.2 Magnet Interaction

Figure 3-2 shows the arrangement of magnets in the bi-stable energy harvester design configuration. In addition to the solid levitated magnet, the harvester consists of stationary top and bottom ring magnets and a single layer (cluster) of intermediate (peripheral) magnets fixed around the body of the harvester. The magnetic force acting on the levitated magnet, F_{mag}, is the result of interaction with the middle (peripheral) fixed magnets, F_{cyl} , the stationary top ring magnet, $F_{top} = F_{ring}(z_t)$, and bottom ring magnet, $F_{bot} = F_{ring}(z_b)$, given by

$$F_{mag} = F_{cyl} + F_{top} + F_{bot}. \qquad \textbf{Eq. 3-2}$$

The stationary top and bottom ring magnets were modeled as having uniform magnetization, $\vec{M}_{top} = \vec{M}_{bot} = M\hat{z}$. The scalar magnetic potential generated by a ring magnet located at position, z_r, along the central axis is [56]:

$$\psi(z, z_r) = \frac{1}{4\pi}\int \frac{\vec{M}\cdot d\vec{s}}{|\vec{r} - \vec{r'}|}$$

$$= \frac{M}{2}\left(\int_a^b \frac{\rho d\rho}{\sqrt{\left(z - z_r - \frac{h}{2}\right)^2 + \rho^2}} - \int_a^b \frac{\rho d\rho}{\sqrt{\left(z - z_r + \frac{h}{2}\right)^2 + \rho^2}}\right) \qquad \textbf{Eq. 3-3}$$

$$= \frac{M}{2}\left(\sqrt{\rho^2 + (z - z_r - h/2)^2} - \sqrt{\rho^2 + (z - z_r + h/2)^2}\right)\Big|_{\rho=a}^{\rho=b}.$$

The magnetic flux density component along the z-axis is then obtained and given by

$$B(z, z_r) = -\mu_0 \frac{d\psi(z, z_r)}{dz}$$

$$= \frac{B_{rf,ring}}{2}\left(\frac{z - z_r + \frac{h}{2}}{\sqrt{\rho^2 + \left(z - z_r + \frac{h}{2}\right)^2}} - \frac{z - z_r - \frac{h}{2}}{\sqrt{\rho^2 + \left(z - z_r - \frac{h}{2}\right)^2}}\right)\Bigg|_{\rho=a}^{\rho=b}, \qquad \textbf{Eq. 3-4}$$

where the magnetization is represented through the residual flux density of a ring magnet, i.e., $M = B_{rf,ring}/\mu_0$. The magnetic force due to a ring magnet is then given by $F_{ring}(z_r) = m_{lev}\ \partial_z B(z, z_r)$ and expressed as

$$F_{ring}(z_r) = \frac{B_{rf,ring}B_{rf,lev}V}{2\mu_0}\left(\frac{a^2}{(a^2+(z_r-z+h/2)^2)^{3/2}} + \frac{b^2}{(b^2+(z_r-z-h/2)^2)^{3/2}} - \frac{a^2}{(a^2+(z_r-z-h/2)^2)^{3/2}} - \frac{b^2}{(b^2+(z_r-z+h/2)^2)^{3/2}}\right), \quad \textbf{Eq. 3-5}$$

where the magnetic moment of the levitated magnet is $m_{lev} = B_{rf,lev}V/\mu_0$. Therefore, the magnetic forces acting on the levitated magnet as a result of the top ring magnet, $F_{top} = F_{ring}(z_t)$, and bottom ring magnet, $F_{bot} = F_{ring}(z_b)$ are given by

$$F_{top} = F_{ring}(z_r = z_t) = \frac{B_{rf,ring}B_{rf,lev}V}{2\mu_0}\left(\frac{a^2}{(a^2+(z_t-z+h/2)^2)^{3/2}} + \frac{b^2}{(b^2+(z_t-z-h/2)^2)^{3/2}} - \frac{a^2}{(a^2+(z_t-z-h/2)^2)^{3/2}} - \frac{b^2}{(b^2+(z_t-z+h/2)^2)^{3/2}}\right), \quad \textbf{Eq. 3-6}$$

and

$$F_{bot} = F_{ring}(z_r = z_b)$$

$$= \frac{B_{rf,ring} B_{rf,lev} V}{2\mu_0} \left(\frac{a^2}{(a^2 + (z_b - z + h/2)^2)^{3/2}} \right.$$

$$+ \frac{b^2}{(b^2 + (z_b - z - h/2)^2)^{3/2}} \qquad \textbf{Eq. 3-7}$$

$$- \frac{a^2}{(a^2 + (z_b - z - h/2)^2)^{3/2}}$$

$$\left. - \frac{b^2}{(b^2 + (z_b - z + h/2)^2)^{3/2}} \right),$$

respectively.

For the bi-stable configuration, we considered a cluster of middle (peripheral) cylindrical solid magnets ($n = 10$) fixed around the body of the harvester as shown in **Figure 3-2**. Since the peripheral magnets were very small compared to the overall size of the harvester the z-component of magnetic flux density generated by these magnets at a given position of the levitated magnet can be approximated as a point magnetic dipole, given by

$$B_{cyl} = n \cdot \frac{\mu_0 m_{cyl}}{4\pi} \frac{2\left(z - z_{cyl}\right)^2 - {\rho_{mid}}^2}{\left({\rho_{mid}}^2 + \left(z - z_{cyl}\right)^2\right)^{5/2}}. \qquad \textbf{Eq. 3-8}$$

The magnetic force is then given by $F_{cyl} = m_{lev}\, \partial_z B_{cyl}(z)$ and can be written as

$$F_{cyl} = \frac{3n\, B_{rf,lev} m_{cyl} V}{4\pi} \frac{(3\rho_{mid}^2 - 2(z - z_{cyl})^2)(z - z_{cyl})}{(\rho_{mid}^2 + (z - z_{cyl})^2)^{7/2}}, \qquad \textbf{Eq. 3-9}$$

where m_{cyl} is the magnetic dipole moment of each middle (peripheral) magnet at an axial position, $z_{cyl} = 0$, and a radial position, ρ_{mid}.

Substituting **Eq. 3-9** and **Eq. 3-7** into **Eq. 3-2** yields the total magnetic force, F_{mag}, for the bi-stable harvester:

$$F_{mag} = \frac{3n\, B_{rf,lev} m_{cyl} V}{4\pi} \frac{(3\rho_{mid}^2 - 2z^2)z}{(\rho_{mid}^2 + z^2)^{7/2}} + \frac{B_{rf,ring} B_{rf,lev} V}{2\mu_0} \left(\frac{a^2}{(a^2+(z_b - z + h/2)^2)^{3/2}} + \frac{b^2}{(b^2+(z_b - z - h/2)^2)^{3/2}} - \frac{a^2}{(a^2+(z_b - z - h/2)^2)^{3/2}} - \frac{b^2}{(b^2+(z_b - z + h/2)^2)^{3/2}} \right) + \frac{B_{rf,ring} B_{rf,lev} V}{2\mu_0} \left(\frac{a^2}{(a^2+(z_t - z + h/2)^2)^{3/2}} + \frac{b^2}{(b^2+(z_t - z - h/2)^2)^{3/2}} - \frac{a^2}{(a^2+(z_t - z - h/2)^2)^{3/2}} - \frac{b^2}{(b^2+(z_t - z + h/2)^2)^{3/2}} \right). \quad \textbf{Eq. 3-10}$$

The interactions between levitated and fixed magnets in the energy harvester provide an inherently nonlinear restoring magnetic force, F_{mag}, that is given by **Eq. 3-10**. Furthermore, the magnetic forces of both harvester configurations, i.e., mono-stable and bi-stable configurations, were simulated using COMSOL software. The AC/DC module in COMSOL Multiphysics software (COMSOL 5.2) was used to simulate the magnetic forces using a two-dimensional (2D) axisymmetric model. In this 2D-model simulation, magnets were represented by rectangles along the plane, and all remaining edges of each magnet were magnetically insulated. A moving mesh function was used upon model simulation of the levitated magnet as it oscillated between the fixed magnets. A parametric sweep was used to estimate the magnetic restoring force as a result of the oscillatory motion of the levitated magnet. The governing equation for the COMSOL model simulation was based on Ampere's law. The relative tolerance was set to 5e-5.

The nonlinear magnetic restoring force, F_{mag}, obtained using **Eq. 3-10** is then integrated into the energy harvester's equation of motion **Eq. 3-10**, yielding

$$m\ddot{x} + c\dot{z} - \frac{3n\, B_{rf,lev} m_{cyl} V}{4\pi} \frac{(3\rho_{mid}^2 - 2z^2)z}{(\rho_{mid}^2 + z^2)^{7/2}} - \frac{B_{rf,ring} B_{rf,lev} V}{2\mu_0} \left(\frac{a^2}{\left(a^2 + \left(z_b - z + \frac{h}{2}\right)^2\right)^{3/2}} + \frac{b^2}{\left(b^2 + \left(z_b - z - \frac{h}{2}\right)^2\right)^{3/2}} - \frac{a^2}{\left(a^2 + \left(z_b - z - \frac{h}{2}\right)^2\right)^{3/2}} - \frac{b^2}{\left(b^2 + \left(z_b - z + \frac{h}{2}\right)^2\right)^{3/2}} \right) - \frac{B_{rf,ring} B_{rf,lev} V}{2\mu_0} \left(\frac{a^2}{\left(a^2 + \left(z_t - z + \frac{h}{2}\right)^2\right)^{3/2}} + \frac{b^2}{\left(b^2 + \left(z_t - z - \frac{h}{2}\right)^2\right)^{3/2}} - \frac{a^2}{\left(a^2 + \left(z_t - z - \frac{h}{2}\right)^2\right)^{3/2}} - \frac{b^2}{\left(b^2 + \left(z_t - z + \frac{h}{2}\right)^2\right)^{3/2}} \right) + mg = 0. \quad \textbf{Eq. 3-11}$$

Adding $-m\ddot{y}$ to both sides of **Eq. 3-11** yields

$$m\ddot{z} + c\dot{z} - \frac{3n\, B_{rf,lev} m_{cyl} V}{4\pi} \frac{(3\rho_{mid}^2 - 2z^2)z}{(\rho_{mid}^2 + z^2)^{7/2}} - \frac{B_{rf,ring} B_{rf,lev} V}{2\mu_0} \left(\frac{a^2}{\left(a^2 + \left(z_b - z + \frac{h}{2}\right)^2\right)^{3/2}} + \frac{b^2}{\left(b^2 + \left(z_b - z - \frac{h}{2}\right)^2\right)^{3/2}} - \frac{a^2}{\left(a^2 + \left(z_b - z - \frac{h}{2}\right)^2\right)^{3/2}} - \frac{b^2}{\left(b^2 + \left(z_b - z + \frac{h}{2}\right)^2\right)^{3/2}} \right) - \frac{B_{rf,ring} B_{rf,lev} V}{2\mu_0} \left(\frac{a^2}{\left(a^2 + \left(z_t - z + \frac{h}{2}\right)^2\right)^{3/2}} + \frac{b^2}{\left(b^2 + \left(z_t - z - \frac{h}{2}\right)^2\right)^{3/2}} - \frac{a^2}{\left(a^2 + \left(z_t - z - \frac{h}{2}\right)^2\right)^{3/2}} - \frac{b^2}{\left(b^2 + \left(z_t - z + \frac{h}{2}\right)^2\right)^{3/2}} \right) + mg = -m\ddot{y}. \quad \textbf{Eq. 3-12}$$

For a harmonic input of the form $\ddot{y} = A.\sin(\omega t)$, where A and ω are acceleration input level and driving frequency, respectively, **Eq. 3-12** becomes

$$\ddot{z} + \frac{c}{m}\dot{z} - \frac{3n\, B_{rf,lev} m_{cyl} V}{4\pi m} \frac{\left(3\rho_{mid}^2 - 2z^2\right)z}{\left(\rho_{mid}^2 + z^2\right)^{7/2}} -$$

$$\frac{B_{rf,ring} B_{rf,lev} V}{2\mu_0 m}\left(\frac{a^2}{\left(a^2+\left(z_b - z + \frac{h}{2}\right)^2\right)^{3/2}} + \frac{b^2}{\left(b^2+\left(z_b - z - \frac{h}{2}\right)^2\right)^{3/2}} - \frac{a^2}{\left(a^2+\left(z_b - z - \frac{h}{2}\right)^2\right)^{3/2}} -\right.$$

$$\left.\frac{b^2}{\left(b^2+\left(z_b - z + \frac{h}{2}\right)^2\right)^{3/2}}\right) - \frac{B_{rf,ring} B_{rf,lev} V}{2\mu_0 m}\left(\frac{a^2}{\left(a^2+\left(z_t - z + \frac{h}{2}\right)^2\right)^{3/2}} + \right. \qquad \textbf{Eq. 3-13}$$

$$\left.\frac{b^2}{\left(b^2+\left(z_t - z - \frac{h}{2}\right)^2\right)^{3/2}} - \frac{a^2}{\left(a^2+\left(z_t - z - \frac{h}{2}\right)^2\right)^{3/2}} - \frac{b^2}{\left(b^2+\left(z_t - z + \frac{h}{2}\right)^2\right)^{3/2}}\right) + g =$$

$$-A.\sin(\omega t).$$

In the mono-stable energy harvester configuration, there were no intermediate (peripheral) magnets, i.e., $F_{cyl} = 0$ and only two stationary top and bottom ring magnets were present. This lack of peripheral magnets resulted in a single stable position and a magnetic force expressed as:

$$F_{mag} = F_{top} + F_{bot}$$

$$= \frac{B_{rf,ring} B_{rf,lev} V}{2\mu_0}\left(\frac{a^2}{(a^2+(z_b - z + h/2)^2)^{3/2}} + \frac{b^2}{(b^2+(z_b - z - h/2)^2)^{3/2}} -\right.$$

$$\left.\frac{a^2}{(a^2+(z_b - z - h/2)^2)^{3/2}} - \frac{b^2}{(b^2+(z_b - z + h/2)^2)^{3/2}}\right) + \qquad \textbf{Eq. 3-14}$$

$$\frac{B_{rf,ring} B_{rf,lev} V}{2\mu_0}\left(\frac{a^2}{(a^2+(z_t - z + h/2)^2)^{3/2}} + \frac{b^2}{(b^2+(z_t - z - h/2)^2)^{3/2}} - \frac{a^2}{(a^2+(z_t - z - h/2)^2)^{3/2}} -\right.$$

$$\left.\frac{b^2}{(b^2+(z_t - z + h/2)^2)^{3/2}}\right).$$

Consequently, using **Eq. 3-2**, the equation of motion for the mono-stable harvester configuration becomes

$$\ddot{z}+\frac{c}{m}\dot{z}-\frac{B_{rf,ring}B_{rf,lev}V}{2\mu_0 m}\left(\frac{a^2}{\left(a^2+\left(z_b-z+\frac{h}{2}\right)^2\right)^{3/2}}+\frac{b^2}{\left(b^2+\left(z_b-z-\frac{h}{2}\right)^2\right)^{3/2}}\right.$$

$$\left.-\frac{a^2}{\left(a^2+\left(z_b-z-\frac{h}{2}\right)^2\right)^{3/2}}-\frac{b^2}{\left(b^2+\left(z_b-z+\frac{h}{2}\right)^2\right)^{3/2}}\right)$$

$$-\frac{B_{rf,ring}B_{rf,lev}V_{lev}}{2\mu_0 m}\left(\frac{a^2}{\left(a^2+\left(z_t-z+\frac{h}{2}\right)^2\right)^{3/2}}+\frac{b^2}{\left(b^2+\left(z_t-z-\frac{h}{2}\right)^2\right)^{3/2}}\right.$$

$$\left.-\frac{a^2}{\left(a^2+\left(z_t-z-\frac{h}{2}\right)^2\right)^{3/2}}-\frac{b^2}{\left(b^2+\left(z_t-z+\frac{h}{2}\right)^2\right)^{3/2}}\right)+g=-A.\sin(\omega t). \quad \textbf{Eq. 3-15}$$

Previous studies used higher order polynomials of the form $K_1 z + K_3 z^3 + K_5 z^5$ to describe these nonlinearities through magnetic stiffness coefficients, K_1, K_3, K_5. Unlike these previous studies, the work presented here develops the analytical expressions for the associated magnetic forces. These analytical expressions are, then, integrated into the harvester's equation of motion (**Eq. 3-1**) for both bi-stable and mono-stable configurations, i.e., **Eq. 3-13** and **Eq. 3-15**, respectively. This integration of the analytical expression of the magnetic force into the equation of motion is essential for understanding the dynamic behavior of these systems as discussed in Section 2.1. Thus, another advantage of this work is its ability to investigate the dynamic and static behavior of the proposed harvester in light of its design parameters including size, shape, separation distance, number of magnets, and number of stable points. The equations of motion derived for both bi-stable (**Eq. 3-13**) and mono-stable (**Eq. 3-15**) configurations are used to simulate the motion of the levitated magnet in response to external harmonic

excitation. Consequently, these simulation results can be used to calculate the open-circuit voltage as discussed next.

3.2.3 Small Displacement Approximation

If the central levitated magnet experiences a small peak-to-peak displacement from the equilibrium point ($z = 0$), the magnetic force given by **Eq. 4** can be expanded using Taylor series expansion leading to a polynomial of the form:

$$F_{mag} \approx -(k_1 z + k_3 z^3), \qquad \textbf{Eq. 3-16}$$

where the coefficients of expansion k_1 and k_3 represent the linear and nonlinear stiffness coefficients, respectively. These coefficients usually are obtained through fits with experimental data. Here, we obtained the explicit analytical formulations in terms of the harvester design parameters, i.e.

$$k_1 = \frac{12\, B_{rf,ring} B_{rf,lev} V}{\mu_0}\left(\frac{a^2(h-H)}{(a^2+(h-H)^2)^{5/2}} + \frac{a^2(h+H)}{(a^2+(h+H)^2)^{5/2}} - \frac{b^2(h-H)}{(b^2+(h-H)^2)^{5/2}} - \frac{b^2(h+H)}{(b^2+(h+H)^2)^{5/2}}\right) \qquad \textbf{Eq. 3-17}$$

and

$$k_3 = \frac{40\, B_{rf,ring} B_{rf,lev} V}{\mu_0}\left(\frac{b^2(h+H)(3b^2-4(h+H)^2)}{(b^2+(h+H)^2)^{9/2}} + \frac{b^2(3b^2-4(h-H)^2)(h-H)}{(b^2+(h-H)^2)^{9/2}} - \frac{a^2(3a^2-4(h-H)^2)(h-H)}{(a^2+(h-H)^2)^{9/2}} - \frac{a^2(h+H)(3a^2-4(h+H)^2)}{(a^2+(h+H)^2)^{9/2}}\right), \qquad \textbf{Eq. 3-18}$$

respectively.

3.2.4 Open Circuit Voltage

When the harvester is externally excited, the kinetic energy of the levitated magnet is converted into electric energy as a result of variation in magnetic flux, ϕ, across a surrounding coil. The induced electromotive force in the coil is given by [56]:

$$\mathcal{E}_c = -\frac{d\phi}{dt} = -\sum_{i=1}^{N_c} \frac{d\phi_i}{dt}. \qquad \textbf{Eq. 3-19}$$

In **Eq. 3-19** the magnetic flux, ϕ, is the sum of magnetic fluxes, ϕ_i, going through each single coil turn. Since the magnetic field due to the fixed magnets does not contribute to the induced electromotive force across the coil, the only contribution is due to the motion of the levitated magnet. The z-component of the magnetic flux density generated by the levitated magnet at position z_i of a single coil turn, i, is [56]:

$$B_z(z_i, \rho) = \frac{\mu_0\, m_{lev}}{4\pi} \frac{2(z_i - z)^2 - \rho^2}{(\rho^2 + (z_i - z)^2)^{5/2}}. \qquad \textbf{Eq. 3-20}$$

Using **Eq. 3-20** the magnetic flux through a single coil turn is given by

$$\phi_i = 2\pi \int_0^{\rho_{coil}} B_z(z_i, \rho)\rho d\rho = \frac{B_{rf,lev}V}{2} \frac{{\rho_{coil}}^2}{({\rho_{coil}}^2 + (z - z_i)^2)^{3/2}}. \qquad \textbf{Eq. 3-21}$$

Thereby, the total flux is

$$\phi = \frac{B_{rf,lev}V}{2} \sum_{i=0}^{N_c-1} \frac{{\rho_{coil}}^2}{({\rho_{coil}}^2 + (z - z_i)^2)^{3/2}}. \qquad \textbf{Eq. 3-22}$$

If N_c is sufficiently large, we can reduce the sum into an integral form and obtain

$$\phi \approx \frac{B_{rf,lev}\mathrm{V}}{2} \int_{\mathrm{z_{coil}}-L}^{\mathrm{z_{coil}}+L} \frac{\rho_{\mathrm{coil}}{}^2\, dz_i}{(\rho_{\mathrm{coil}}{}^2 + (\mathrm{z} - \mathrm{z_i})^2)^{\frac{3}{2}}}$$

$$= \frac{B_{rf,lev}\mathrm{VN_c}}{4\mathrm{L}} \left(\frac{\mathrm{L} - \mathrm{z} + \mathrm{z_{coil}}}{\sqrt{\rho_{\mathrm{coil}}{}^2 + (\mathrm{L} - \mathrm{z} + \mathrm{z_{coil}})^2}} \right. \qquad \textbf{Eq. 3-23}$$

$$\left. + \frac{\mathrm{L} + \mathrm{z} - \mathrm{z_{coil}}}{\sqrt{\rho_{\mathrm{coil}}{}^2 + (\mathrm{L} + \mathrm{z} - \mathrm{z_{coil}})^2}} \right).$$

Substituting **Eq. 3-23** into **Eq. 3-19** yields

$$\mathcal{E}_c = \frac{B_{rf,lev}\mathrm{VN_c}\rho_{\mathrm{coil}}{}^2}{4\mathrm{L}} \left(\frac{1}{(\rho_{\mathrm{coil}}{}^2 + (\mathrm{L} - \mathrm{z} + \mathrm{z_{coil}})^2)^{3/2}} \right.$$

$$\left. - \frac{1}{(\rho_{\mathrm{coil}}{}^2 + (\mathrm{L} + \mathrm{z} - \mathrm{z_{coil}})^2)^{3/2}} \right) \dot{\mathrm{z}}. \qquad \textbf{Eq. 3-24}$$

The induced electromotive force in the top and bottom coil sections, $\mathcal{E}$, is composed of the electromotive force in the top coil section, $\mathcal{E}_1 = \mathcal{E}_c(z_{coil} = z_{ct})$, and the bottom coil section, $\mathcal{E}_2 = -\mathcal{E}_c(z_{coil} = z_{cb})$; the negative sign in $\mathcal{E}_2$ accounts for the opposite winding directions of the top coil and the bottom coil. The total induced electromotive force can be written as

$$\mathcal{E} = \frac{B_{rf,lev}\mathrm{VN_c}\rho_{\mathrm{coil}}{}^2}{4\mathrm{L}}\left(\frac{1}{(\rho_{\mathrm{coil}}{}^2 + (\mathrm{L} - \mathrm{z} + \mathrm{z_{ct}})^2)^{3/2}} - \frac{1}{(\rho_{\mathrm{coil}}{}^2 + (\mathrm{L} + \mathrm{z} - \mathrm{z_{ct}})^2)^{3/2}} - \frac{1}{(\rho_{\mathrm{coil}}{}^2 + (\mathrm{L} - \mathrm{z} + \mathrm{z_{cb}})^2)^{3/2}} + \frac{1}{(\rho_{\mathrm{coil}}{}^2 + (\mathrm{L} + \mathrm{z} - \mathrm{z_{cb}})^2)^{3/2}}\right)\dot{\mathrm{z}}. \quad \textbf{Eq. 3-25}$$

3.2.5 Magnetic Damping

When the energy harvester is connected to a load resistance, R_{load}, the current flowing in each coil turn is expressed as

$$I = \pm\frac{\mathcal{E}}{R_{coil} + R_{load}}. \quad \textbf{Eq. 3-26}$$

Due to the opposite winding directions of the top and the bottom coil sections (see **Figure 3-2**) the current I is defined as positive if it belongs to the top coil section and negative if it belongs to the bottom coil. The magnetic field produced by each coil turn is expressed as [56]:

$$\mathrm{B_i} = \frac{\mu_0\, I\, \rho_{\mathrm{coil}}{}^2}{2((z_s - \mathrm{z_i})^2 + \rho_{\mathrm{coil}}{}^2)^{3/2}}. \quad \textbf{Eq. 3-27}$$

The force acting on the levitated magnet as a result of this magnetic field is expressed as

$$F_i = m_{lev}\left.\frac{\partial B_i}{\partial z_s}\right|_{z_s=z} = \frac{3\rho_{\mathrm{coil}}{}^2 I m_{lev}(\mathrm{z_i} - \mathrm{z})\mu_0}{2(\rho_{\mathrm{coil}}{}^2 + (\mathrm{z_i} - \mathrm{z})^2)^{5/2}}. \quad \textbf{Eq. 3-28}$$

The total magnetic damping force is obtained by integrating the force component over all coil turns in the two coil sections and is given by

$$F_{eddy} = \frac{N_c}{2L}\left(\int_{z_{ct}-L}^{z_{ct}+L} F_i\, dz_i + \int_{z_{cb}-L}^{z_{cb}+L} F_i\, dz_i\right)$$

$$= \frac{\rho_{\mathrm{coil}}{}^4 B_{rf,lev}^2 \mathrm{V}^2 N_c{}^2 \dot{z}}{2L^2(R_{load}+R_{coil})}\left(-\frac{1}{\left(\rho_{\mathrm{coil}}{}^2+\left(L+(z_{ct}-\mathrm{z})\right)^2\right)^{3/2}}\right.$$

$$+\frac{1}{\left(\rho_{\mathrm{coil}}{}^2+\left(L+(z_{cb}-\mathrm{z})\right)^2\right)^{3/2}}+\frac{1}{\left(\rho_{\mathrm{coil}}{}^2+\left(L-(z_{ct}-\mathrm{z})\right)^2\right)^{3/2}}$$

$$\left.-\frac{1}{\left(\rho_{\mathrm{coil}}{}^2+\left(L-(z_{cb}-\mathrm{z})\right)^2\right)^{3/2}}\right)\left(\frac{1}{\left(\rho_{\mathrm{coil}}{}^2+\left(L+(z_{ct}-\mathrm{z})\right)^2\right)^{3/2}}\right.$$

$$-\frac{1}{\left(\rho_{\mathrm{coil}}{}^2+\left(L+(z_{cb}-\mathrm{z})\right)^2\right)^{3/2}}-\frac{1}{\left(\rho_{\mathrm{coil}}{}^2+\left(L-(z_{ct}-\mathrm{z})\right)^2\right)^{3/2}}$$

$$\left.+\frac{1}{\left(\rho_{\mathrm{coil}}{}^2+\left(L-(z_{cb}-\mathrm{z})\right)^2\right)^{3/2}}\right) = \mathrm{C(z)}\,\dot{\mathrm{z}}.$$

Eq. 3-29

The magnetic damping force, F_{eddy}, can be approximated by the following model, where C_m is simply the global maximum of C(z):

$$\mathrm{F_{eddy}} = \mathrm{C_m}\,\dot{\mathrm{z}}$$

Eq. 3-30

3.2.6 Electrical Power

The magnetic damping force F_{eddy} given by **Eq. 3-29** is substituted into the equation of motion (**Eq. 3-1**), which is then solved numerically using the 4th and the 5th order Runge-Kutta method that is implemented in MATLAB ODE45 solvers. The obtained solution is then substituted into **Eq. 3-25** to obtain the voltage on the surrounding coils. The model prediction of the generated power is then calculated from **Eq. 3-25** and given by

$$P = \frac{\mathcal{E}^2\, R_{load}}{(R_{load}+R_{coil})^2}.$$

Eq. 3-31

CHAPTER 4

FABRICATION AND EXPERIMENT

This chapter goes over the experimental process that validates our dynamic and electrodynamic models. **Section 4.1** discusses the fabrication of the energy harvester and the ability to switch from mono-stable mode to bi-stable mode. Also, **Section 4.1** details the material and design of each component in our device and how all the components can be assembled together. **Section 4.2** discusses the experimental setup that includes the magnetic force measurement in **Section 4.2.1,** and the dynamic characterization in **Section 4.2.2. Section 4.2** details the names and model numbers of all of our measuring equipment used to perform our experiments and the procedures of the experiments. This chapter incorporates work from four publications by the author, previously published in November 2018 [20], November 2019 [21], February 2020 [22], and April 2020 [23]. It is reproduced here with the permission from all the coauthors involved in this study.

4.1 Fabrication

To validate the derived models and get a fundamental grasp of important design parameters, an energy harvester prototype was created and experimentally characterized. The prototype of the constructed energy harvester prototype is shown in **Figure 4-1**. A polylactic acid (PLA) thermoplastic filament was used to manufacture the harvester's housing. Through the 3D-printed center (peripheral) magnet holder, the implemented design enables for switching from a mono-stable to bi-stable configuration. Dimensions,

material characteristics, and geometries of both mono-stable and bi-stable configurations studied in this study are listed in **Table 4-1**.

Table 4-1: Geometric and material properties of the fabricated harvester.

Parameter	Mono-stable	Bi-stable
Number of middle (peripheral) magnets, n	0	10
Coil resistance (R_{coil}) (Ω)	207	
Load resistance (R_{Load}) (Ω)	207	
Total number of coil turns	1000	
Number of coil turns in top or bottom coil sections, N_c	500	
Coil material	Copper, 40 AWG	
Levitated magnet size (height×diameter) (mm)	12.7×12.7	
Levitated magnet material	NdFeB-N52	
Stationary ring top and bottom magnets size (Outer diameter×Inner diameter×height) (mm)	$25.4 \times 12.7 \times 12.7$	
Stationary ring top and bottom magnets material	NdFeB-N42	
Stationary middle (peripheral) magnets size (height×diameter) (mm)	0.79375×4.7625	
Stationary middle (peripheral) magnets material	NdFeB-N42	
Casing material	Polylactic acid (PLA)	

The harvester's major components were CAD developed using SolidWorks software. The top magnet holder (**Figure 4-1**a), bottom magnet holder (**Figure 4-1**b), core inside which the levitated magnet was captured (**Figure 4-1**c), peripheral magnet cap and peripheral magnet holder (**Figure 4-1**d-e), and the base were the components (**Figure 4-1**f-h). After that, the files were sent to a 3D printer, which was used to construct the harvester's primary components. Two ring magnets were put into the top magnet holder and the bottom magnet holder to repel the levitated magnet during the assembly of the harvester. To establish bi-stability, the layer of peripheral magnet holder (**Figure 4-1**e) was put directly into the core; a cap was 3D printed to secure the layer of peripheral magnets in place (**Figure 4-1**). The harvester's mono-stable state can likewise

be restored by removing the layer. Screw threads were used to connect the top and bottom magnet holders to the core. During the dynamic tests, a base comprised of two components was used to grab the bottom of the harvester firmly while maintaining a safe distance between the harvester and the shaker table.

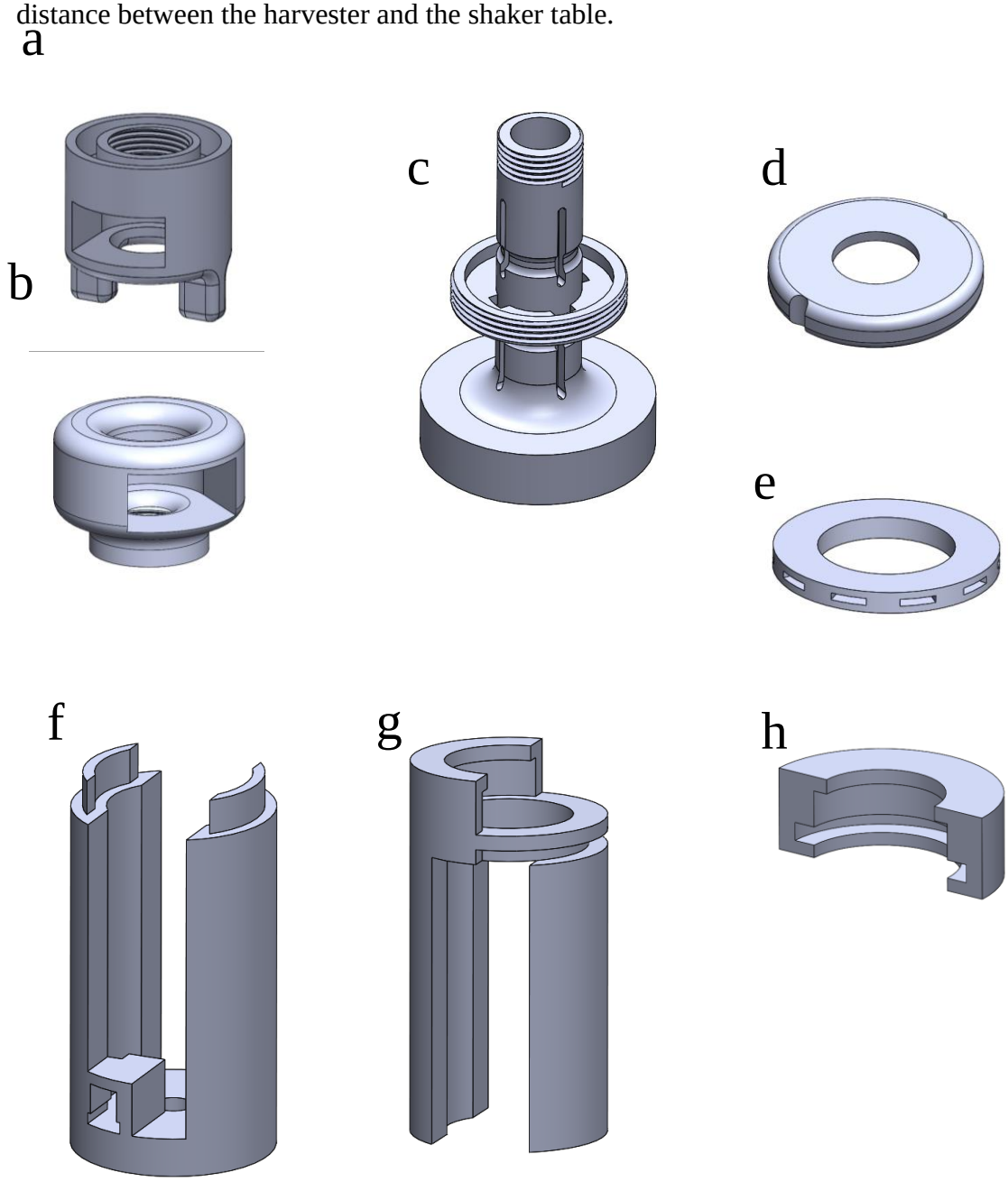

Figure 4-1: All components of the energy harvester fabricated drawn with the SolidWorks software containing: (a) Top-magnet holder, (b) Bottom-magnet holder, (c) Core, (d) Peripheral-magnet cap, (e) Peripheral-magnet holder, (f, g, h) Base.

The stationary magnets were chosen as NdFeB-N42 ring magnets because the ring design not only allows air to move freely, reducing mechanical damping, but also makes displacement measurement easier during dynamic tests. Because of its great strength and symmetrical shape, a NdFeB-N52 cylindrical magnet was employed as the levitated magnet. Ten microscopic NdFeB-N42 magnets were implanted into the 3D printed structure illustrated in **Figure 3-1**e to create the layer of peripheral magnets. **Figure 3-1**e shows a printed ring that not only keeps the peripheral magnets in place, but also makes insertion and removal of the layer of peripheral magnets easier.

The core had two indentation sections to hold the two copper coils in place, minimizing the radius of the copper coils. The periphery magnetic holder separated the two coils, which were coiled in opposite directions to maximize the output voltage. To achieve a smooth printing process, all printed components were manufactured from PLA (3D Universe, 2.85 mm). Sandpapers of varying roughness were used to clear the interior of the harvester body illustrated in **Figure 4-1**c to make the inner surface of the core smooth so that the levitated magnet could travel with ease. **Figure 4-2**a and **Figure 4-2**b show the manufactured energy harvester in mono-stable and bi-stable configurations, respectively.

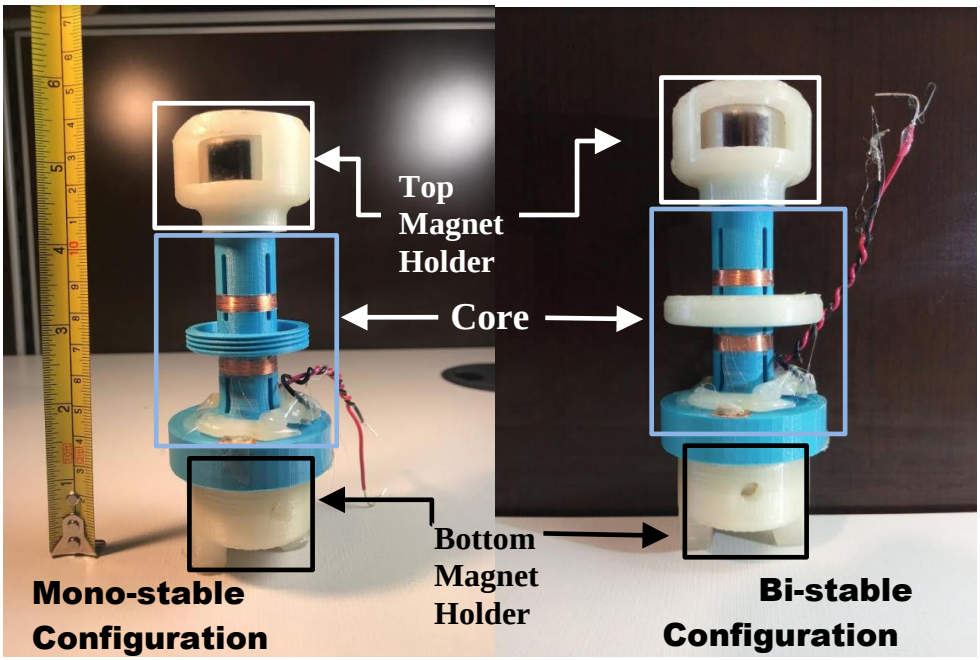

Figure 4-2: The (a) mono-stable and the (b) bi-stable configurations of the energy harvester; the base is not presented. The peripheral-magnet cap can be seen in the bi-stable configuration.

4.2 Experimental Setup

4.2.1 Magnetic Force

A test platform (SHIMPO FGS-250W), a displacement sensor (KEYENCE IL-100), and a digital force sensor (SHIMPO FG-3006) were used to detect the repulsive magnetic force, as illustrated in **Figure 4-3** and **Figure 4-4**. A data acquisition system (NI myDAQ) was used to record both displacement and force readings, which were then saved on a PC. The energy harvester's design included fixed top and bottom ring magnets, which allowed the displacement of the levitated magnet to be measured using the laser signal from the displacement sensor. The harvester was fastened to the test stand's base to measure magnetic forces, and a brass rod was placed into the harvester from the top. The response force was reported by connecting one end of the brass rod to the levitated magnet and the other end to the force sensor. The force sensor was also

connected to the laser sensor to allow the brass rod and the laser sensor to move in lockstep. The test stand's hand wheel was used to control the force sensor's movement. The relative movement of the levitated magnet was detected by the laser sensor as it measured the distance between itself and an object mounted to the test platform. The reaction force and relative displacement may be read from the force gauge and laser sensor LCD screens, respectively, and entered into an Excel sheet. The laser sensor was powered by a DC power supply, while the force gauge was powered by a PC via USB cable.

The entire arrangement, which included the test platform, harvester, force gauge, brass rod, and laser sensor, could be adjusted horizontally to eliminate gravity's effect. The levitated magnet's equilibrium positions were recorded so that the force curve could be plotted using the relative displacement data. The force was measured on one side of the harvester at a time; the harvester was taken from the test stand, reversed in direction, then glued back to the test platform to measure the other side.

The levitated magnet lying on the side of the tube generated friction when the setup was rotated horizontally during the force-displacement measurement. However, because the frictional force was small (on the scale of 0.01 N) in comparison to the magnetic force (on the order of 1 N), the effect of friction was minimal. Furthermore, moving the arrangement horizontally eliminated the requirement to measure the levitated magnet's shift in displacement due to gravity, making the force-displacement measurement easier.

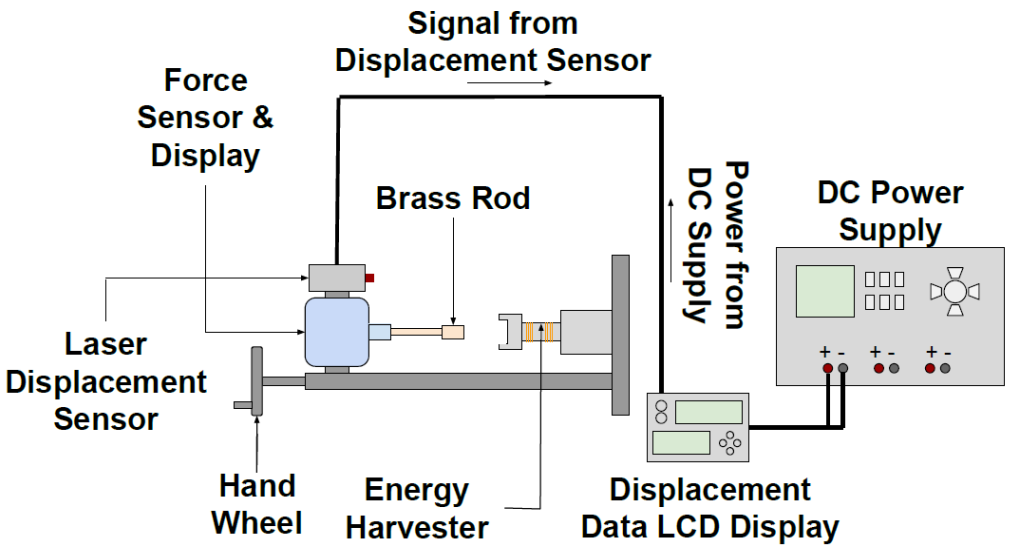

Figure 4-3: Diagram of the experimental setup used to measure nonlinear magnetic restoring forces of the levitated magnet.

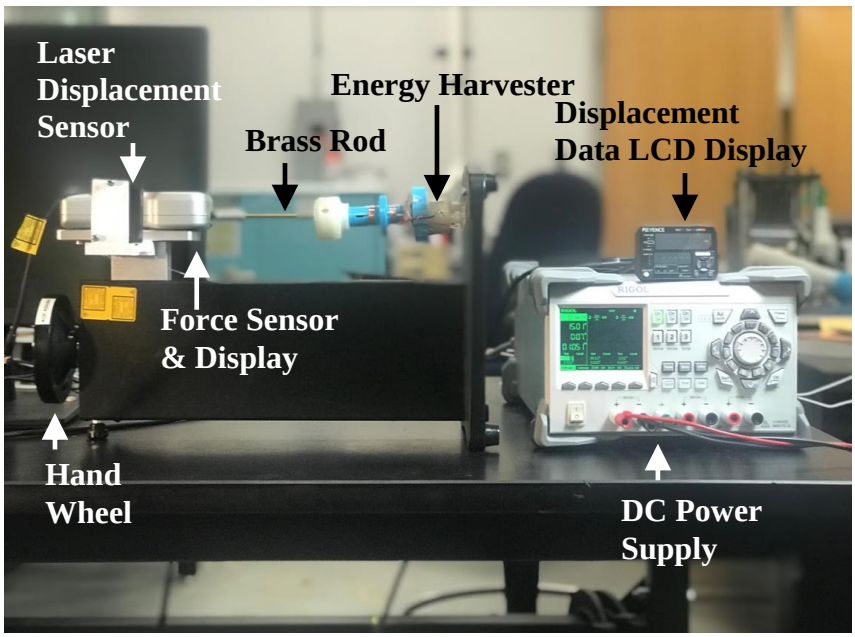

Figure 4-4: An image of the experimental setup used to measure nonlinear magnetic restoring forces of the levitated magnet.

4.2.2 Dynamic Characterization

The experimental setup used to characterize the energy harvesters in dynamic mode is shown in **Figure 4-5** and **Figure 4-6**. A shaker table (VT-500, SENTEK

DYNAMICS), a power amplifier (LA-800, SENTEK DYNAMICS), a vibration controller (S81B-P02, SENTEK DYNAMICS), an accelerometer (PCB333B30 model, PCB Piezotronics), a data collecting system (NI myDAQ), and a computer make up the setup. The harvester was firmly attached on the shaker table's surface, and its response to specified frequencies and accelerations was measured. A 3D-printed base was used to attach the energy harvester to the shaker table's armature. The energy harvester was firmly held at the top of the base, while the armature was attached to the bottom of the base through a stud. The controller was connected to an accelerometer that was linked to the base. The shaker table was controlled by the controller, which was connected to the power amplifier, which was connected to the shaker table. The shaker table's motion was controlled by the Engineering Data Management (EDM) software, which allowed for accurate input of the acceleration and sweeping frequencies. To measure the open-circuit output voltage, the two ends of the coils are linked to the data logger. A load resistor was attached in parallel to the coils for close-circuit output power measurements (not shown in **Figure 4-5**). A laser sensor positioned on top of the harvester measures the displacement of the levitated magnet. The data recorder was also connected to the laser. The LabVIEW program was used to read the data from the coils and the laser. The vibration of the shaker table was swept at 1.25 g from 10 Hz to 30 Hz in the mono-stable configuration, and at 2.5 g from 15 Hz to 35 Hz in the bi-stable configuration.

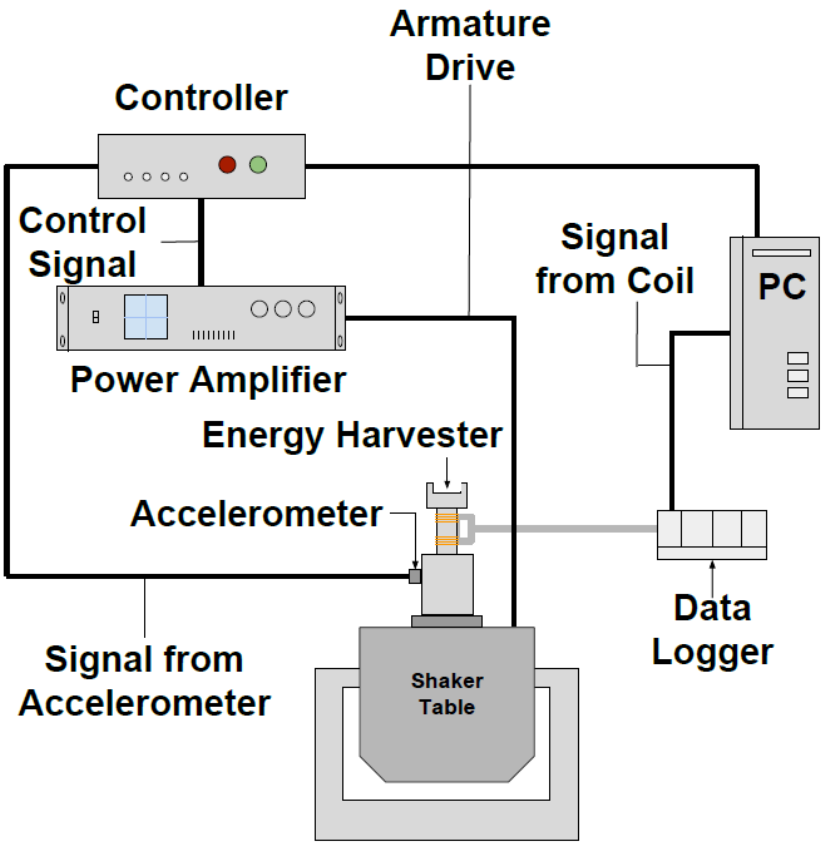

Figure 4-5: Diagram of the experimental setup used for dynamic characterization of the fabricated energy harvester.

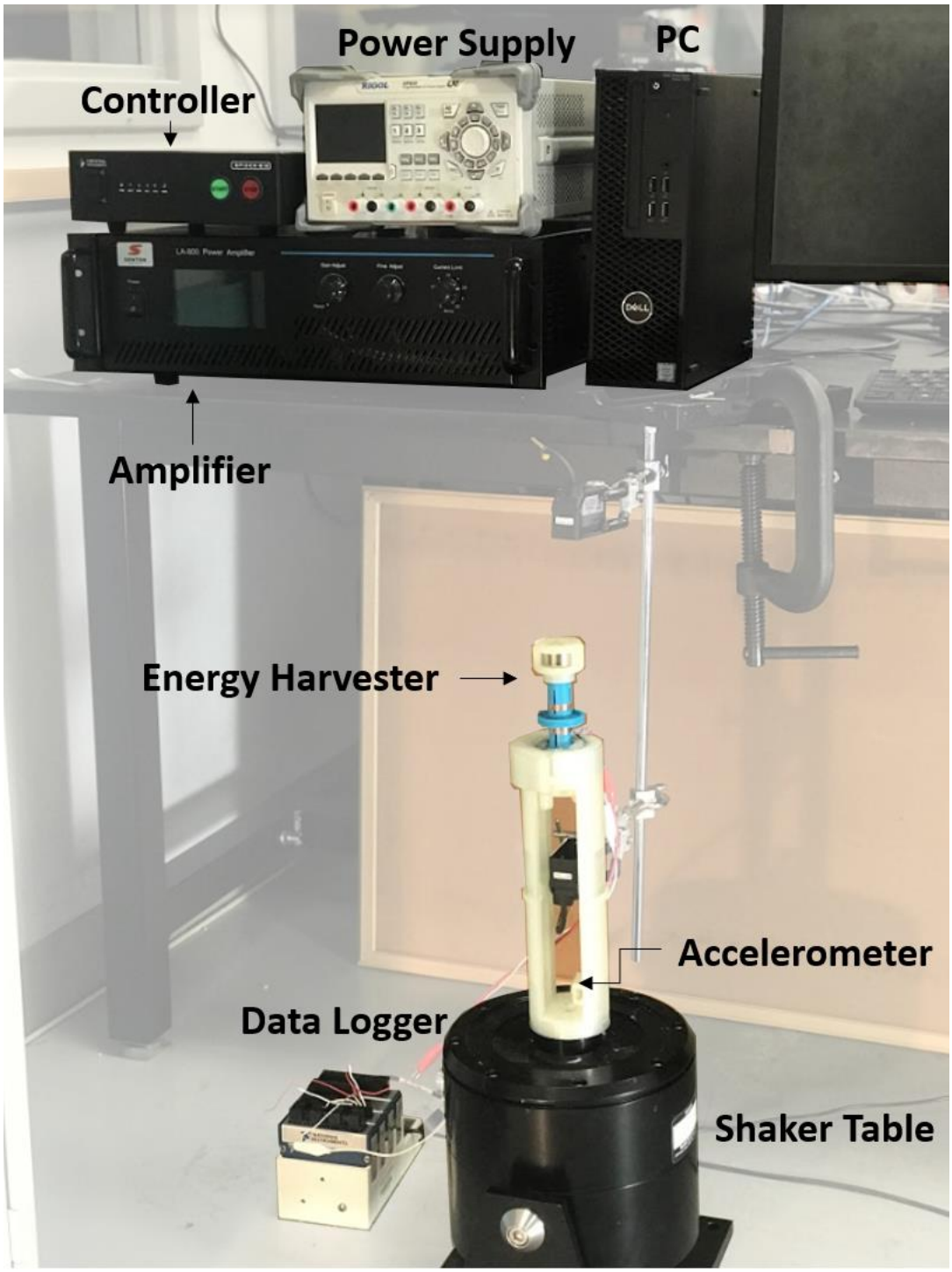

Figure 4-6: An image of the experimental setup used for dynamic characterization of the fabricated energy harvester.

CHAPTER 5

RESULTS AND DISCUSSION

This chapter mainly focuses on the validation of the developed models presented in Chapter 2. Parameters used in the validation process are recorded in the APPENDIX. **Section 4.1** discusses the differences in the dynamic of the mono-stable and the bi-stable spring system. **Section 4.1.1** reports the model validation of the mono-stable and bi-stable spring system. The validation includes the magnetic force models, open circuit voltage models, phase portrait diagrams, and power generation models. **Section 4.1.2** presents a parametric study to investigate the effect of thickness of the peripheral magnets on the performance of the harvester. **Section 4.2** delves into the parametric study of the mono-stable spring system. **Section 4.2.1** discusses the effect of each design parameter on the linear and nonlinear stiffness terms of the spring system. **Section 4.2.2** shift the focus onto the magnetic damping effect. Finally, **Section 4.2.3** discusses about the effect of the design parameters on the power generation of the energy harvester. This chapter incorporates work from four publications by the author, previously published in November 2018 [20], November 2019 [21], February 2020 [22], and April 2020 [23]. It is reproduced here with the permission from all the coauthors involved in this study.

5.1 Monostable Vs. Bistable

5.1.1 Model Validation

Magnetic Force and Potential Energy Wells

The magnetic force created between the solid levitated magnet and the fixed magnets was simulated using COMSOL software, calculated with the developed magnetic force model (**Eq. 3-10** and **Eq. 3-14**), and measured empirically with the experimental apparatus illustrated in **Figure 5-1**. For both mono-stable and bi-stable configurations, **Figure 5-1**a and **Figure 5-1**b compare findings from the COMSOL simulations and analytical model to experimentally measured magnetic forces. Both the COMSOL simulations and the analytical model matched the measured data very well. The restoring magnetic forces exhibit nonlinear behavior. In **Figure 5-1**a, the force-displacement curve displays a single equilibrium position around the origin point, i.e. (0, 0). The restoring force curve in **Figure 5-1**b, on the other hand, has three zero force points. These coordinates relate to one unstable equilibrium position (0, 0), as well as two nearby stable positions. In some areas, the force-displacement graphs have negative slopes, indicating negative stiffness. As a result, when the levitated magnet entered the negative stiffness region, it tended to gravitate toward the nearest stable equilibrium point, which was between (8.69,0) and (-8.69,0) mm. **Figure 5-1**a and **Figure 5-1**b exhibit fifth-order polynomial fits of the form $K_1z+K_3z^3+K_5z^5$ for both mono-stable and bi-stable situations, respectively. The polynomial fit matches the experimental data for the mono-stable arrangement fairly well, according to the results (**Figure 5-1**a). The polynomial fit from measured data and model predictions deteriorates dramatically for

the bi-stable arrangement (**Figure 5-1**b). Furthermore, the data imply that the difference gets worse as the displacement increases.

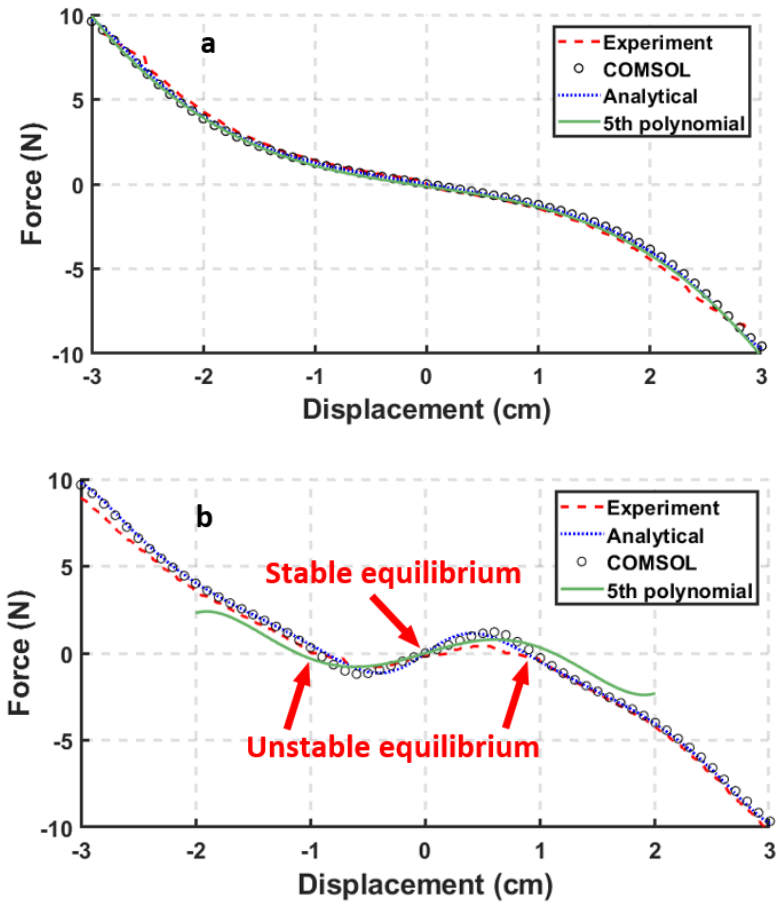

Figure 5-1: The diagrams of a) the magnetic restoring forces in the mono-stable configuration measured experimentally and obtained using models and b) the magnetic restoring forces in the bi-stable configuration measured experimentally and obtained using models.

The resolution of the force gauge and the displacement sensor are the sources of error. The force gauge and displacement sensor have resolutions of 0.01 N and 0.1 mm, respectively. We determined that the resolutions of the two sensors were sufficient for carrying out the experiment since the magnetic force and displacement ranges are around -10 N to 10 N and -30 mm to 30 mm, respectively.

After obtaining the polynomial function using methods such as least-square regression, it can be integrated into **Eq. 3-1** to solve for the velocity of the levitated magnet. Because of its simplicity and low processing effort, polynomial fit is frequently utilized. However, as seen in **Figure 5-1**b, polynomial fitting does not work well for some experimental datasets; in these circumstances, analytical approaches are utilized to better describe the experimental behavior at the cost of increasing the complexity of **Eq. 3-1**. As a result, the analytical method is employed to improve the polynomial fit method's accuracy.

The magnetic potential-energy wells for both mono-stable and bi-stable energy harvesters produced using $U = - F_{mag}\, dz$ are shown in **Figure 5-3** and **Figure 5-4**. The number and position of the middle magnets holder determine the transition from mono-stable to bi-stable. The potential energy diagrams in **Figure 5-2**a and **Figure 5-2**b, for example, illustrate single-well and double-well curves, which correspond to mono-stable and bi-stable energy harvesters, respectively. There was only one stable position for the levitated magnet between the fixed, top and bottom magnets in the absence of the middle (peripheral) magnet holder, i.e., a single well curve as illustrated in **Figure 5-2**a. The levitated magnet was pushed to travel towards one of two stable places when the middle (peripheral) magnet holder was clamped around the harvester casing. As a result, as illustrated in **Figure 5-2**b, two symmetric potential energy wells separated by one hilltop saddle were constructed.

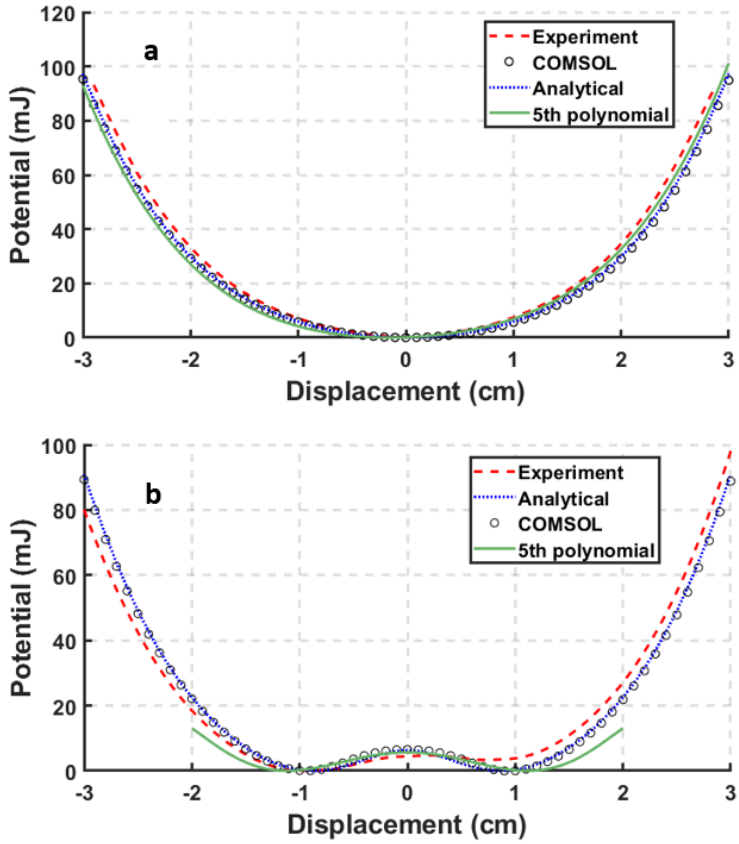

Figure 5-2: The diagrams of a) the potential-energy wells and barriers of the fabricated energy harvesters in the mono-stable configuration measured experimentally and obtained using models, and b) the potential-energy wells and barriers of the fabricated energy harvester in the bi-stable configuration measured experimentally and obtained using models.

Open Circuit Voltage and Frequency Response

During both forward and backward sweeping, open-circuit voltage measurements and model simulations for the mono-stable energy harvester arrangement are illustrated in **Figure 5-3**. **Eq. 3-21** was used to generate model simulations. **Figure 5-1** also shows the findings obtained using the force polynomial fit. The voltage-frequency responses generated using the model, polynomial fit, and measured data are consistent with the results. Both forward and backward sweeping revealed the stiffening frequency response. The nonlinearities in the magnetic spring stiffness experienced by the harvester produce

this hardening phenomenon. This nonlinear behavior led in a hysteresis zone surrounded by a forward and backward frequency leap, 16.9 Hz and 14.5 Hz, respectively, as illustrated in **Figure 5-3**. [57]. In addition, when compared to forward sweeping, backward sweeping had a lower amplitude in frequency response. During forward sweeping, the induced voltage grew in proportion to the frequency until it peaked at 16.9 Hz. Due to the coexistence of two stable states at the frequency branch [58], i.e., high energy state against low energy state, this climax was followed by a frequency drop down. This dynamic behavior is known as the frequency jump or saddle-node point phenomenon, and it is a distinctive feature of nonlinear Duffing oscillators [30], [59]. The frequency response of the harvester was non-resonant as a result of the frequency jump and hysteresis. Model simulations and observed data both indicate hardening effects, frequency jump phenomena, and magnitude of frequency response, as illustrated in **Figure 5-3**.

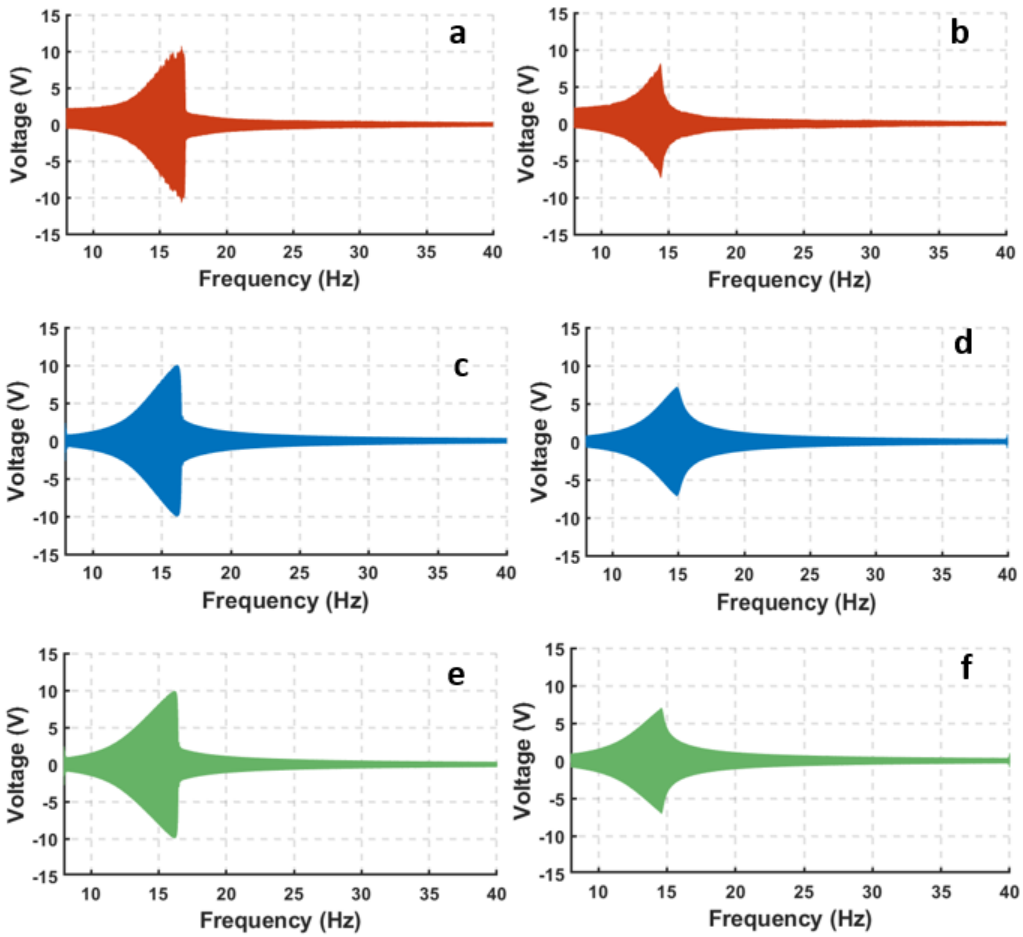

Figure 5-3: Open-circuit voltage envelope of the mono-stable configuration obtained at $1.25\ \mathrm{g\,m\,s^{-2}}$ a) Forward experiment b) Backward experiment, c) Forward model, d) Backward model, e) Forward, using polynomial fit, and f) Backward, using polynomial fit.

The frequency response of the bi-stable energy harvester was calculated using the experiment, model, and magnetic force polynomial fit, as shown in **Figure 5-4**. The harvester's frequency sweep experiment reveals a softening frequency response. Model simulations (**Figure 5-4**c-d) differed slightly from the experiment (**Figure 5-4**a-b), but the model's force-displacement curve matched the experimental data, as shown in **Figure 5-1**a. For example, whereas the frequency jump predicted by the model (**Figure 5-4**c) closely matches the experiment (**Figure 5-4**a) during forward sweeping, there was a 1 Hz shift in frequency jump predicted by the model (**Figure 5-4**d) during backward sweeping

compared to the observation (**Figure 5-4**b). As a result, a few factors connected to the dynamic test setup and experiment may be to blame for the extremely minor difference between model predictions and measured results. Several studies, including Dong *et al*. [60], Lee *et al*. [29], Berdy *et al*. [25], and Dhote *et al*. [61], have observed similar discrepancies between model simulation and measured results for nonlinear Duffing-type oscillators [61]. The difference between the model and the experiment, for example, could be explained by the presence of a minor tilt in the levitated magnet, which could cause multi-direction vibration, increased damping, and blockage of vertical movement of the levitated magnet [25]. This mismatch is apparently due to geometric misalignment of the energy harvester when agitated using the shaker table during the experiment, as Dhote *et al*. [61] pointed out. This geometric misalignment causes the levitated magnet to move in the radial direction, resulting in the generation of additional magnetic force components. As a result, new vibration modes start up. Despite this, the developed model in this study did not account for these vibration patterns. The occurrence of nonlinear damping [62], experimental error [29], [60], or perhaps the experiment apparatus not perfectly resembling a single-degree-of-freedom system as envisaged in our model could all account for the modest discrepancy [60].

Nonetheless, as shown in **Figure 5-4**a-d, both the model and the experiment follow similar patterns and exhibit similar properties, such as frequency-jump occurrences, hardness and softening effects, and frequency-response amplitudes. When comparing results from model predictions to the results obtained using the magnetic force polynomial fit (**Figure 5-4**e-f), we can see that the polynomial fit (**Figure 5-4**e-f) has a poorer match and larger deviations from the measured data (**Figure 5-4**a-b), especially

around the frequency jump during both forward and backward sweeping (**Figure 5-4**a-b). During forward and backward sweeping, the difference between findings derived using the polynomial fit and observed data increased to 3 Hz and 5 Hz, respectively. This disagreement in the resonant frequency was expected since, as shown in **Figure 5-1**b, the magnetic force calculated using the polynomial fit deviated greatly from the experimental data.

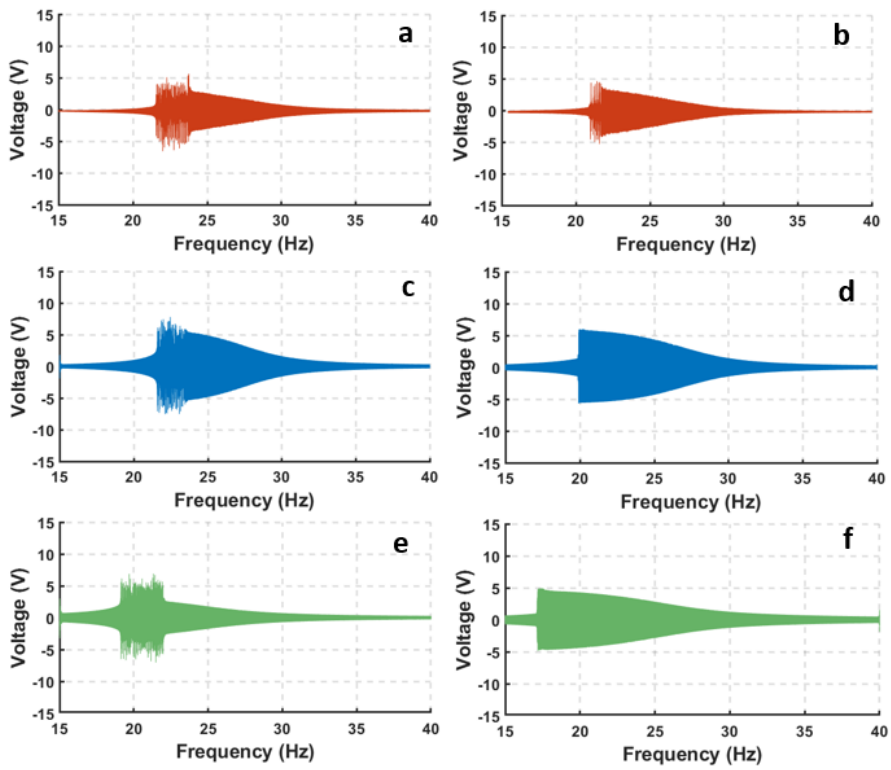

Figure 5-4: Open-circuit voltage envelop of the bi-stable configuration obtained at $2.5\ \mathrm{g\ m\ s^{-2}}$ a) Forward experiment b) Backward experiment, c) Forward model, d) Backward model, e) Forward, using polynomial fit, f) Backward, using polynomial fit.

Phase Portrait Diagram for bistable magnetic spring

Figure 5-5 depicts phase portrait diagrams of the bi-stable energy harvester produced from experiment and model at various frequencies, i.e., 15.0-35.5 Hz, at a fixed acceleration, i.e., 2.5 g m s^{-2}. A displacement sensor was used to track the location of the

levitated magnet in these studies (model: KEYENCE IL-100, not shown in **Figure 4-5**). The results of model simulations were confirmed by experimental data. Dynamical regimes were identified in both model simulations and measured data. The levitated magnet oscillated within a single well at lower frequencies, as seen in **Figure 5-5**a-b, resulting in intra-well oscillation. The levitated magnet continued to oscillate in intra-well mode as the driving frequency rose, but the displacement and velocity increased as well, causing the phase portrait diagram to open up as seen in **Figure 5-5**c-d. **Figure 5-5**e-f shows chaotic oscillation between the two wells after the levitated magnet generated enough energy to pass the energy barrier. Once the harvester crossed the frequency leap, the chaotic oscillation was replaced by intra-well oscillation, as seen in **Figure 5-5**g-h. As the harvester was excited at higher frequencies, both velocity and displacement decreased, and the phase portrait diagram shrank, as shown in **Figure 5-5**i-j

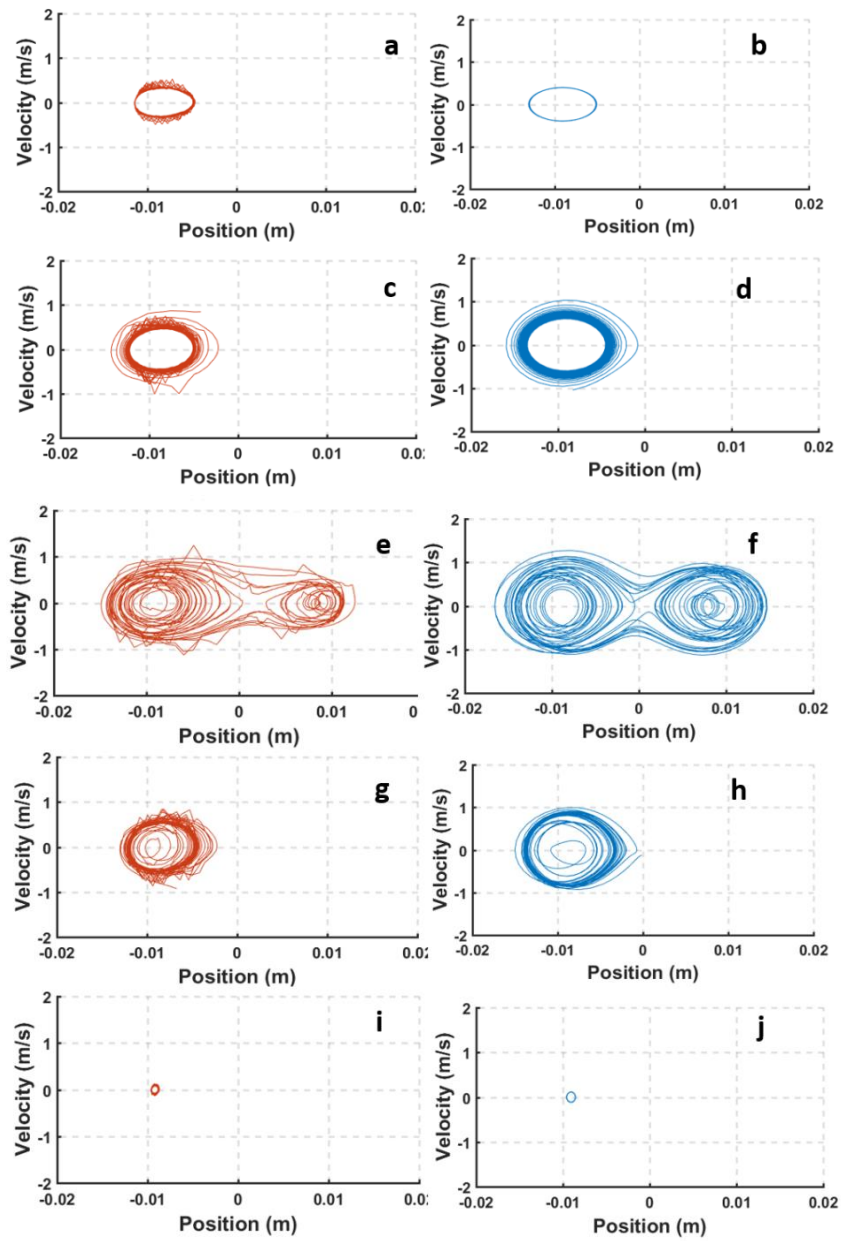

Figure 5-5: Phase portrait of the bi-stable energy harvester obtained at 2.5 g m s^{-2} a) Experiment and b) model at 15.0-15.5 Hz; c) Experiment and d) Model at 21.0-21.5 Hz, e) Experiment and f) Model at 22.5-23.0 Hz; g) Experiment and h) Model at 23.8-24.3 Hz; i) Experiment and j) Model at 35.0-35.5 Hz.

Figure 5-6, **Figure 5-7**, and **Figure 5-8** demonstrate the displacement curves of the levitated magnet produced from experiment and model simulations, confirming the phase portrait diagram's behavior. Intra-well and chaotic oscillations occurred in the bi-

stable energy harvester. The harvester encountered intra-well motion and modest displacement amplitudes, velocities, and hence, voltages at lower frequencies while using fixed-base acceleration. When the harvester was aroused around jump frequency, he experienced chaotic motion. **Figure 5-6** and **Figure 5-7** show that inter-well oscillatory motion, which produces large displacement amplitudes and velocities, was not present. Nonetheless, the model (tested at 4 g m s^{-2}) suggests that inter-well motion can be achieved at greater accelerations or by modifying key design parameters (see **Figure 5-8**). The harvester encounters tremendous peak-to-peak displacements and velocities during this inter-well motion, resulting in voltages up to 30 V.

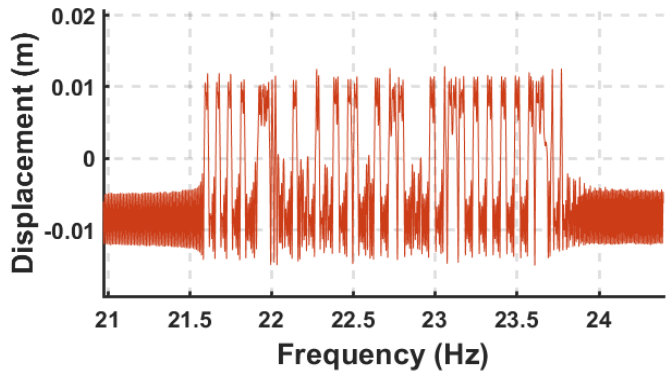

Figure 5-6: Displacement history of the bi-stable energy harvester obtained at 2.5 g m s^{-2} from experimental data.

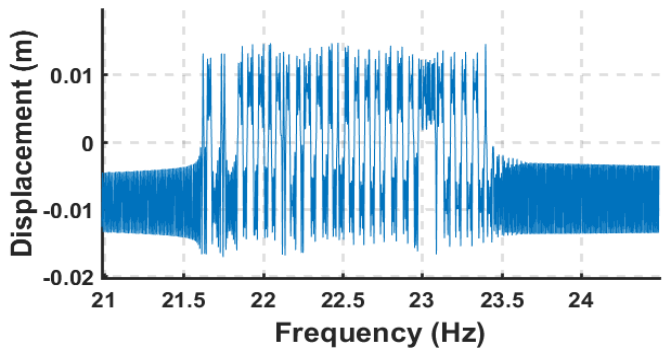

Figure 5-7: Displacement history of the bi-stable energy harvester obtained at 2.5 g m s^{-2} from model prediction.

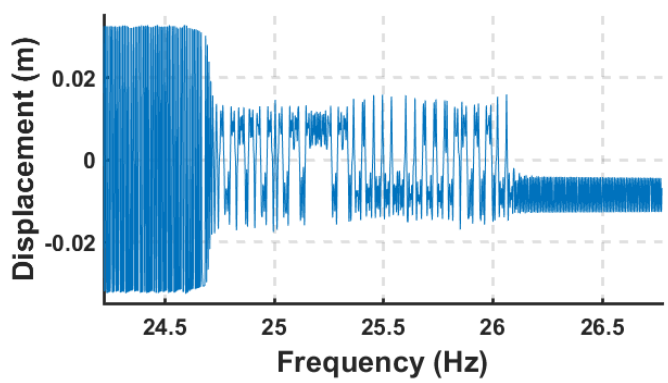

Figure 5-8: Inter-well motion obtained using model prediction at 4.0 g m s^{-2}.

Power Generation

Figure 5-9 and **Figure 5-10** demonstrate power metrics for mono-stable and bi-stable configurations determined using experiment and model. The experimental setup depicted in **Figure 4-5**s was used to detect induced voltage across a load resistance using a decade box (GLOBAL SPECIALTIES RDB-10, not shown in **Figure 4-5**). The output voltage was measured across a load resistance, R_{load}, while the frequencies were swept between 5 and 40 Hz in these studies. **Figure 5-9** and **Figure 5-10** depict the harvester's power density determined at each load resistance, R_{load}, in the range (2, 10^4). The power density of the harvester was normalized against the volume of the harvester and the acceleration level input to the harvester, i.e., $\mathrm{mW\ cm^{-3}\ g^{-2}}$. **Eq. 3-31** was used to generate model simulations.

For both mono-stable and bi-stable energy harvester arrangements, the results illustrated in **Figure 5-9** and **Figure 5-10** match model simulation and measured output power well. Both mono-stable and bi-stable topologies have maximum measured power densities of around 5.0 mW cm(-3) g(-2) and 0.35 mW cm(-3) g(-2), respectively. **Figure 5-9** and **Figure 5-10** show that the maximal power densities for mono-stable and bi-stable setups are roughly 1,000 Ω and 200 Ω, respectively. Magnetic damping, as indicated in **Eq. 3-29**, and the displacement amplitude of the levitated magnet can explain this variation in the optimum load resistance. The displacement amplitude of the levitated magnet in the bi-stable energy harvester configuration is minimal, possibly because the levitated magnet was stuck in one of the two potential energy wells depicted in **Figure 5-2**b. This modest displacement amplitude corresponds to R_{load} = 200 Ω, which correlates to small magnetic damping. The levitated magnet in the mono-stable energy harvester

configuration, on the other hand, had a bigger displacement amplitude and consequently more magnetic damping. Because more load resistance was required to lessen the magnetic damping effects, the optimal load resistance was changed to a higher value, R_{load} = 1,000 Ω.

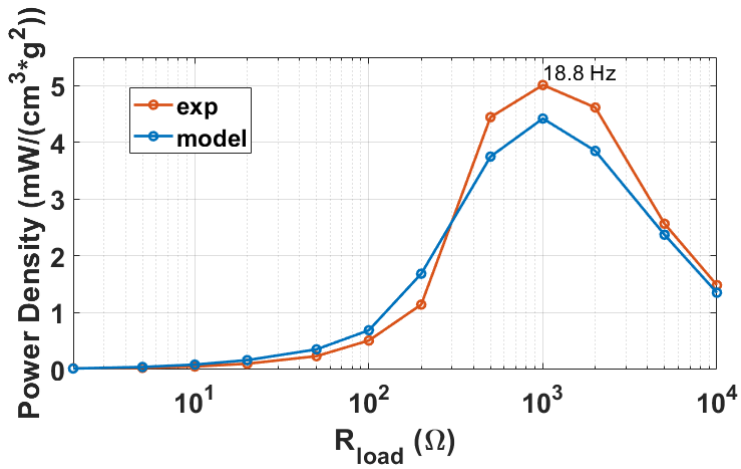

Figure 5-9: Power densities obtained using experiment and model simulation of the mono-stable configuration at 1.25 g m s^{-2}.

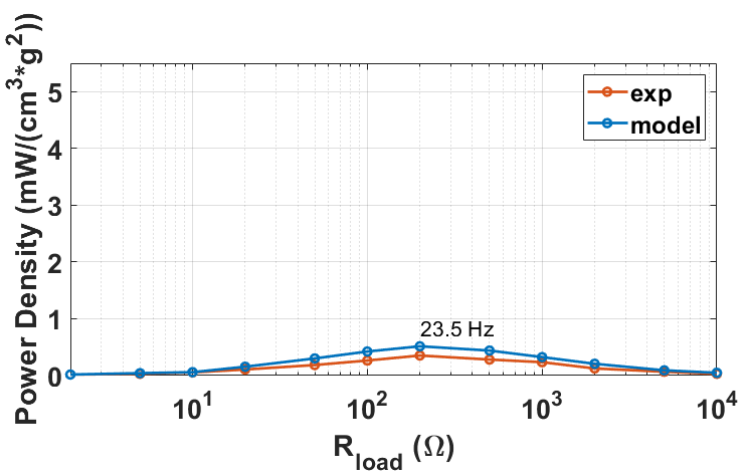

Figure 5-10: Power densities obtained using experiment and model simulation of the bi-stable configuration at 2.5 g m s^{-2}.

Next, using an experiment and a model, the performance and behavior of mono-stable and bi-stable vibration energy harvester topologies when connected to a load resistance were explored. The mono-stable and bi-stable harvester setups were excited at 1.25 g m s^{-2} and 2.5 g m s^{-2}, respectively, for both model simulation and experiment. We can solve **Eq. 3-1** to determine the position of the levitated magnet, z, then substitute the solution into **Eq. 3-19** to obtain the voltage induced into the surrounding coils, and yield model simulations. The experiment setup depicted in **Figure 4-5** was used to detect the induced voltage across a load resistance using a decade box (GLOBAL SPECIALTIES RDB-10, not shown in **Figure 4-5**). The load resistance, R_{load}, was fixed in these trials, and the output voltage was measured while the frequencies were swept between 5 and 40 Hz. Representative examples of voltage-frequency responses obtained for both mono-stable and bi-stable energy harvesters are presented in **Figure 5-11**. These examples were created by combining an experiment and a model with three different load resistances, R_{load} = 100 Ω, 1 kΩ, and 10 kΩ, respectively. **Figure 5-12** shows the peak power obtained at each load resistance for both mono-stable and bi-stable energy harvester designs. Model simulations for output power were generated using **Eq. 3-31** in **Figure 5-12**. For both mono-stable and bi-stable energy harvester arrangements, the results illustrated in **Figure 5-11** and **Figure 5-12** match well with model simulation and observed voltage and output power.

Figure 5-11 and **Figure 5-12** provide a comprehensive overview and key insights into the behavior of mono-stable and bi-stable energy harvesters. According to the results of **Figure 5-11**, increasing load resistance, R_{load}, induced a shift in jump frequency, thus allowing the energy harvesters' response to be tuned to the desired frequency range by

altering the load resistance. Nonetheless, adjusting the load resistance to tune the leaping frequency comes at the expense of power generation. That is, when the load resistance grew, the harvester's power output increased progressively until an optimum load resistance was obtained. Maximum power generation occurs at approximately R_{load} = 1,000 Ω and 200 Ω for mono-stable and bi-stable configurations, respectively, according to **Figure 5-14**. Despite the fact that the mono-stable and bi-stable harvesters are manufactured identically and have the same coil resistance, R_{coil} = 193 Ω, the mono-stable harvester's optimum load resistance, R_{load} = 1,000 Ω, is much higher. Magnetic damping, as mentioned in **Eq. 3-24**, and the displacement amplitude of the levitated magnet can explain this movement of the optimum load resistance away from the coil resistance. The displacement amplitude of the levitated magnet was minimal in the bi-stable energy harvester configuration, likely because the levitated magnet was stuck in one of the two potential energy wells depicted in **Figure 5-14**. This modest displacement amplitude corresponds to R_{load} = 200 Ω, which correlates to small magnetic damping. The levitated magnet in the mono-stable energy harvester configuration, on the other hand, had a bigger displacement amplitude and consequently more magnetic damping. Because more load resistance was required to lessen the magnetic damping effects, the optimal load resistance was changed to a higher value, R_{load} = 1,000 Ω. The peak power density is derived by normalizing the recorded peak power at a certain load resistance against the acceleration level and device volume, as shown in **Figure 5-12**.

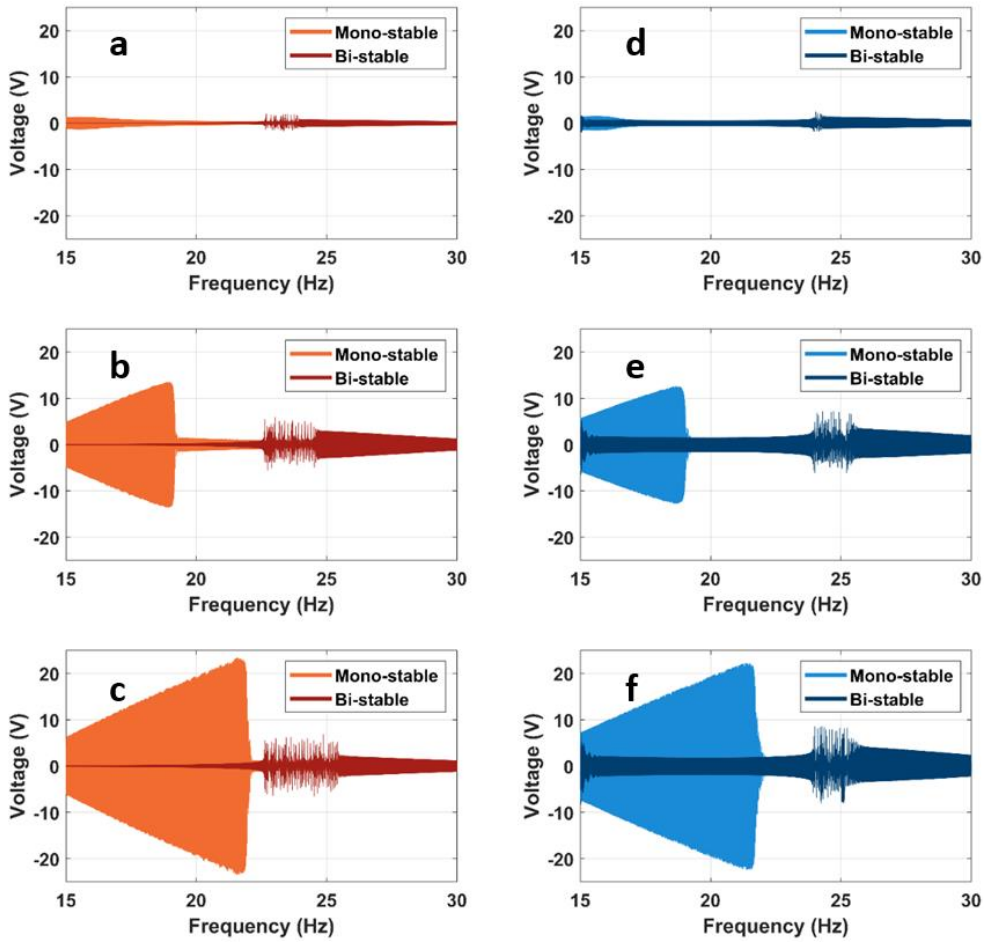

Figure 5-11. Representative examples of model simulation and measured output voltage of the mono-stable and bi-stable energy harvester configurations when connected to load resistance; R_{load} obtained at 1.25 g m s^{-2} for mono-stable and 2.5 g m s^{-2} for bi-stable configuration: (a) Experiment at R_{load} =100 Ω, (b) Experiment at R_{load} =1 kΩ, (c) Experiment at R_{load} =10 kΩ, (d) Model simulations R_{load} =100 Ω, (e) Model simulations R_{load} =1 kΩ, and (f) Model simulations R_{load} =10 kΩ.

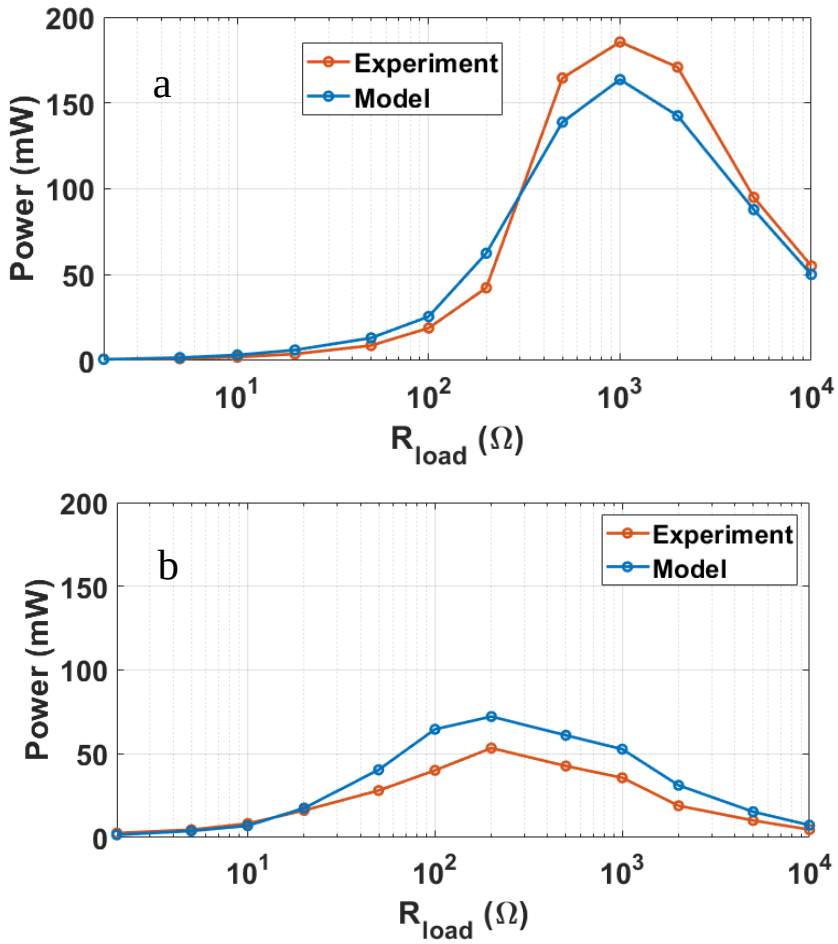

Figure 5-12. Peak power versus load resistance obtained using experiment and model simulation of the a) mono-stable configuration at $1.25\ \mathrm{g\ m\ s^{-2}}$ and b) bi-stable configuration at $2.5\ \mathrm{g\ m\ s^{-2}}$.

5.1.2 Model Simulation and Effect of Design of Bi-stability

The next section discusses the parametric research and implications of different design parameters on the performance and dynamics of the bi-stable energy harvester. The bi-stable vibration energy harvester configuration with a nonlinear magnetic spring was created by combining middle (peripheral) magnets and a levitated magnet in a unique arrangement. The nonlinearities induced by the magnetic spring resulted in a wide range of stiffness characteristics and force-displacement curves, allowing the interplay between the levitated magnet and fixed magnets to represent a wide range of dynamic

regimes. The geometric ratios and size of the peripheral magnets can be adjusted to tailor these nonlinear features.

The force-displacement curves of the bi-stable energy harvester produced for varied geometric ratios of the peripheral magnets are shown in **Figure 5-13** and **Figure 5-14**. The height of the peripheral magnets mounted around the body of the harvester was modified in the range of (1/8, 1/128) inch while the dimensions of the levitated magnet were set at nominal values provided in **Table 4-1**. **Figure 5-13** and **Figure 5-14** show that when thinner peripheral magnets are utilized, the harvester's bi-stability is diminished, and the energy harvester shifts to mono-stable mode. Because the contribution of the peripheral magnets to the total magnetic force decreases as they become thinner, this was expected. As a result, the interaction between the levitated magnet and the top and bottom fixed magnets dominates the magnetic force. Thus, the harvester moves towards mono-stability as suggested in **Figure 5-13** and **Figure 5-14**. When thicker peripheral magnets surround the levitated magnet, the energy harvester suffers higher nonlinearities and larger negative stiffness values, as seen in **Figure 5-13** and **Figure 5-14**. **Figure 5-13** demonstrates, on the other hand, that for very thin peripheral magnets, such as 1/128 inch, the harvester approaches mono-stability and can attain approximately zero stiffness for a particular range of displacements. That is, the harvester experienced approximately zero stiffness for the deflection range of (-5, 5) cm, which is advantageous for energy harvesting at very low frequencies and modest excitation levels. This was also seen in the energy harvester's potential energy curve, as shown in **Figure 5-14**. The harvester energy barrier was flattened and moved towards mono-stability by using 1/128-inch thin peripheral magnets. Stronger stiffness

nonlinearities and energy barriers resulted from thicker peripheral magnets, which pushed the system closer to bi-stability.

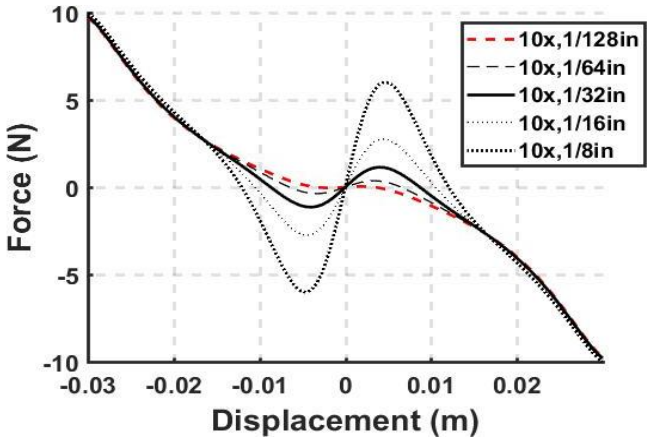

Figure 5-13: Model simulations of the force-displacement curves of the bi-stable energy harvester obtained for different geometric ratios of the peripheral magnets.

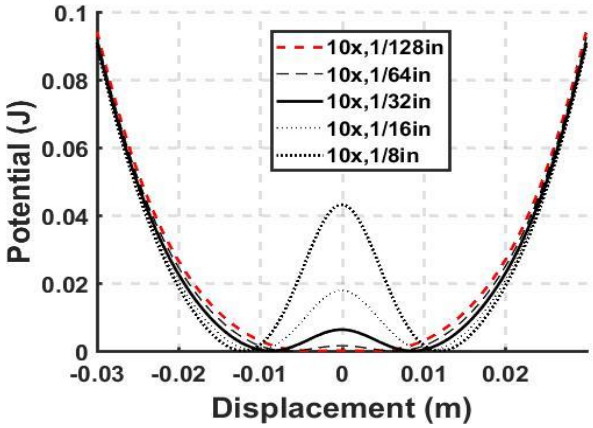

Figure 5-14: Model simulations of the potential-energy wells and barriers of the bi-stable energy harvester obtained for different geometric ratios of the peripheral magnets.

Figure 5-15 illustrates the frequency response of the harvester with thick and thin peripheral magnets, i.e., 1/32 and 1/128 inch, respectively, at different acceleration levels to further study the effect of the peripheral magnets. In different settings, the harvester hardens and softens, according to the findings. For example, during forward sweeping at all acceleration levels, such as 1 g, 3 g, and 5 g (m s^{-2}), a harvester with 1/128 inch

peripheral magnets reacted in a hardening pattern. A harvester with 1/32 inch peripheral magnets, on the other hand, exhibited softening behavior during forward sweeping at 1 g and 3 g (m s^{-2}), as shown in **Figure 5-15**a and **Figure 5-15**c, respectively. At 2.5 g (m s^{-2}), this pattern is identical to that obtained in the experiment and depicted in **Figure 5-5**. Nonetheless, around 5 g (m s^{-2}), the harvester turns to hardening behavior, as seen in **Figure 5-15**e. The force-displacement curves presented in **Figure 5-13** can be used to explain this changeover. The levitated magnet exhibited only intra-well and chaotic dynamics for the 1/32 inch peripheral magnets arrangement at 1 g and 3 g (m s^{-2}), as illustrated in **Figure 5-15**a and **Figure 5-15**c, respectively. The levitated magnet was restricted between -10 and 10 mm and oscillated within the two stable wells. The force experienced by the levitated magnet as it oscillated within this displacement range was very minimal, as illustrated in **Figure 5-15**a's force-displacement curve for the 1/32 inch periphery magnets. As a result, the levitated magnet alternated between these two stable locations slowly.

As a result, the harvester's resonant peak shifted to lower values, and the harvester began to soften. The harvester, on the other hand, showed inter-well motion at a greater acceleration level, such as 5 g (m s^{-2}), as seen in **Figure 5-15**e. The magnet that was levitated oscillated over a wider displacement range. As seen in **Figure 5-15**a, the levitated magnet was subjected to greater forces over this displacement range. Therefore, the levitated magnet oscillated quicker, shifting the resonant peak to a higher value and causing hardening effects. This was likewise confirmed by the reverse sweep. For example, due to the limited travel distances and forces experienced by the levitated magnet, the harvester with thin 1/128 inch periphery magnets displayed softening

behavior during backward sweeping at 1 g ($\mathrm{m\ s^{-2}}$) in **Figure 5-15**b. In addition, **Figure 5-15** shows that a thinner peripheral magnets configuration, such as 1/128 inch, produces a larger frequency response at all acceleration levels than a thick peripheral magnets configuration, such as 1/32 inch.

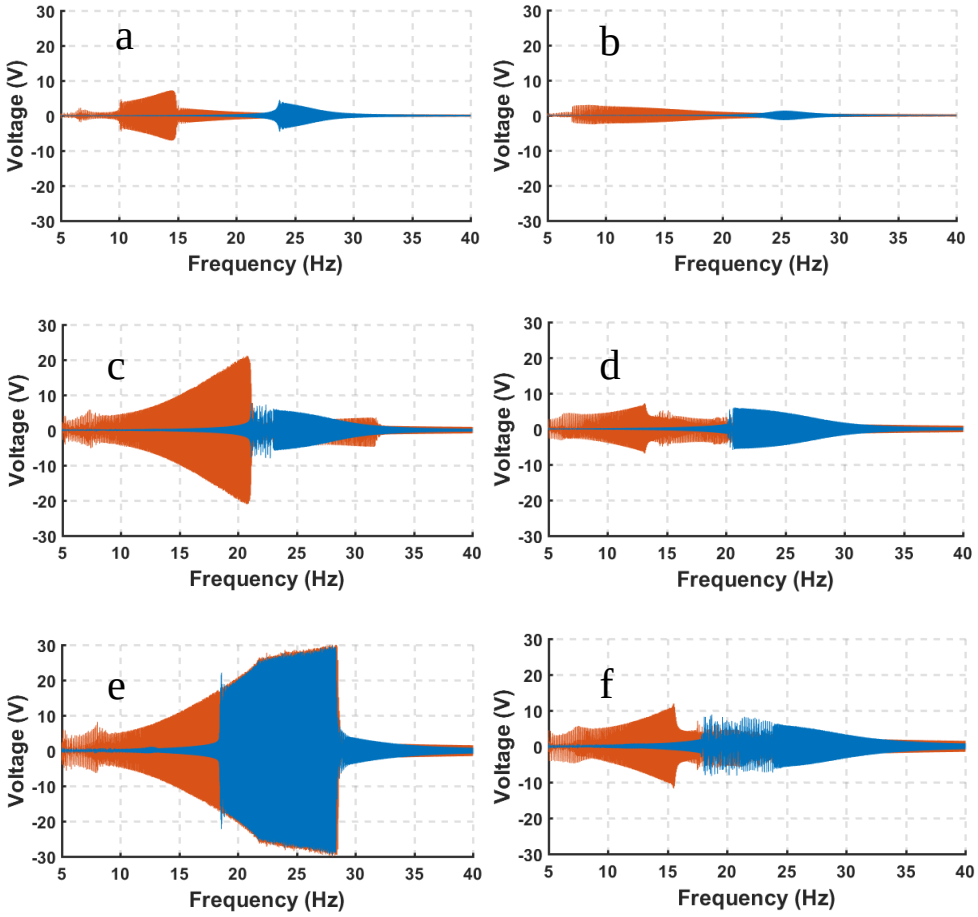

Figure 5-15: Comparison of open-circuit voltage envelop of the bi-stable harvester obtained for 1/32 inch (BLUE) and 1/128 inch (ORANGE) thick peripheral magnets configurations: a) Forward and b) Backward at 1 g m s^{-2}; c) Forward and d) Backward at 3 g (m s^{-2}); e) Forward and f) Backward at 5 g (m s^{-2}).

According to the prior debate, thinner peripheral magnets are better for energy harvester design, especially at lower acceleration levels. Thinner peripheral magnets, on the other hand, produce reduced energy barriers, enhanced frequency responses, and near-zero stiffness behavior at equilibrium, which is advantageous for energy harvesting at low frequencies and low excitation levels. The introduction of thinner peripheral magnets means that the setup is becoming mono-stable. Because of the trend toward mono-stability and the use of thinner peripheral magnets, mono-stability appears to be the most advantageous mode for vibration energy harvesting under harmonic excitation.

5.2 Design of Magnetic Spring

5.2.1 Design Criteria for Stiffness Nonlinearity

The impacts of magnetic spring design parameters on the linear, k_1, and nonlinear, k_3, stiffness coefficients determined using **Eq. 3-17** and **Eq. 3-18**, respectively, are shown in **Figure 5-16**. The volume of the levitated magnet (V), the height of stationary magnets (h), the inner diameter of stationary magnets (a), the outer diameter of stationary magnets (b), and the distance between the two stationary magnets (H) are among the design parameters. The linear and nonlinear stiffness coefficients appear to be linked, according to the findings. Both k_1 and k_3 are proportional to the volume of the levitated magnet (V) and the height of the stationary magnets, for example (h). The magnetic spring force acting on the levitated magnet increases as the volume of the levitated magnet, (V), and the height of each stationary ring magnet, (h), increase, resulting in an increase in the linear and nonlinear stiffness coefficients. On the other hand, k_1 and k_3 are inversely proportional to the stationary magnets' inner diameter (a) and the distance between them (H). Furthermore, as the outer diameter of the stationary ring magnets, (b), grows, the linear and nonlinear stiffness coefficients, k_1 and k_3, rise and decline, with their maximums occurring at two different outer diameter values, as illustrated in **Figure 5-16**d. The nonlinear stiffness coefficient, k_3, becomes zero, i.e. $k_3 = 0$, at a specific value of the outer diameter, b_c, while the linear stiffness coefficient, k_1, stays positive, resulting in a linear magnetic spring. When the outer diameter, b, is less than this critical value, b_c, both the linear and nonlinear stiffness coefficients, k_1, are positive, resulting in a hardening magnetic spring. Finally, when the outer diameter, b, exceeds the critical value, i.e., $b > b_c$, the nonlinear stiffness coefficient, k_3, decreases while the linear

stiffness coefficient, k_1, stays positive, resulting in a softening magnetic spring. As a result, the outer diameter of the stationary ring magnets, b, can be utilized to control the magnetic spring's nonlinearity in order to achieve a linear, hardening nonlinear, or softening nonlinear dynamic response of the energy harvester.

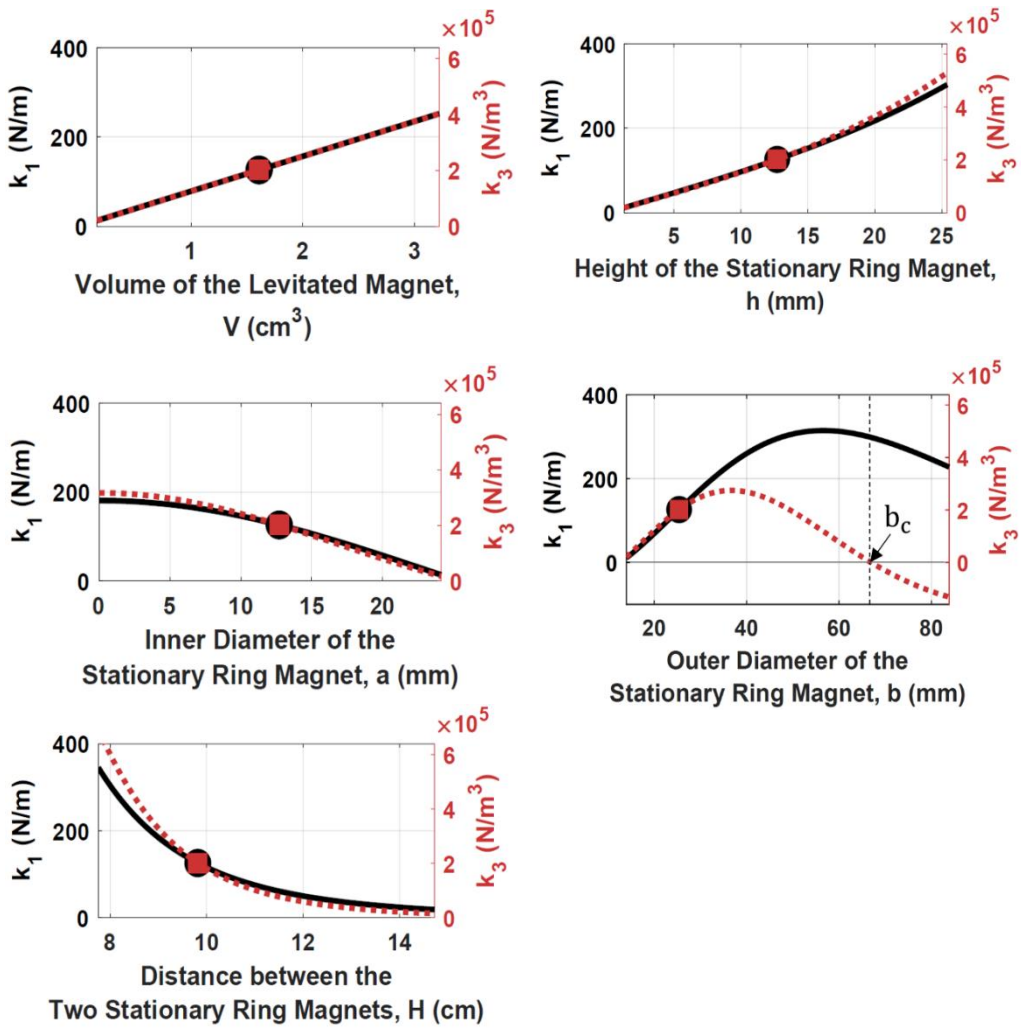

Figure 5-16: Design of linear and nonlinear stiffness coefficients, k_1 and k_3, respectively, with respect to a) volume of the levitated magnet, b) height of the stationary ring magnets, c) inner diameter of the stationary ring magnets, d) outer diameter of the stationary ring magnets, and e) distance between two stationary ring magnets. In the figure, the black circular dot and the red square dot represent the nominal values of k_1 and k_3, respectively, given in the nomenclature table. The solid black line and the dotted red line represent the behavior of k_1 and k_3, respectively, as each parameter changes.

5.2.2 Magnetic Damping

The model simulations for the magnetic damping coefficients obtained using **Eq. 3-29** are shown in **Figure 5-17**. The energy harvester undergoes variable magnetic damping force with two peaks within the two coil sections and two smaller (local)

damping force peaks outside the gap between the two coil sections, as illustrated in **Figure 5-17**. As the levitated magnet passes through the center of each coil segment, the magnetic damping force, F_{eddy}, calculated using the analytical damping model **Eq. 3-29**, falls to zero. As the levitated magnet moves away from the equilibrium location, the magnetic damping force, F_{eddy}, approaches zero. However, as shown in **Figure 5-18**, the simplified magnetic damping coefficient computed using **Eq. 3-30** provides an astute approximation for the total damping in the energy harvester. When the analytical damping model **Eq. 3-29** and the analytical force model (**Eq. 3-14**) are introduced into the equation of motion (**Eq. 3-1**), **Figure 5-18** displays model simulations of induced voltages. The model simulations of the induced voltage obtained when the simplified magnetic damping model (**Eq. 3-30**) and the analytical force model (**Eq. 3-14**) are applied to the equation of motion (**Eq. 3-1**) are also shown in the figure.

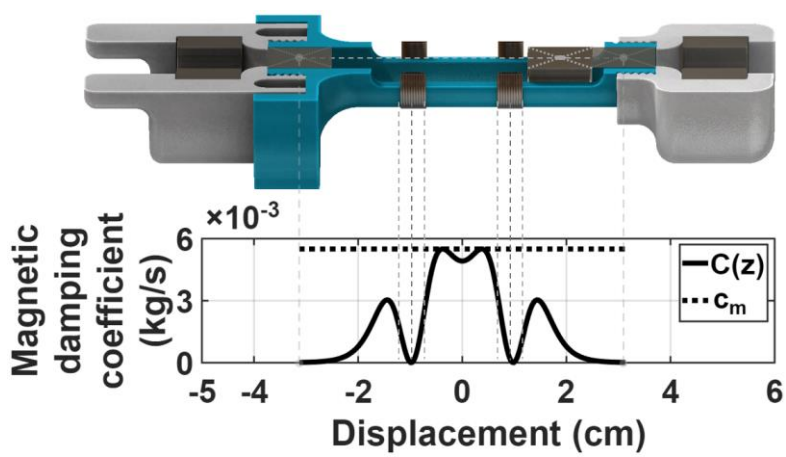

Figure 5-17: Magnetic damping coefficient with respect to displacement, z, obtained using the nominal design parameters given in the nomenclature table. Simulations are performed for acceleration level 1.25 g [m/s^2], load resistance $R_l = 10\ k\Omega$, and $c_m = 5.5 \times 10^{-3}$ kg/s.

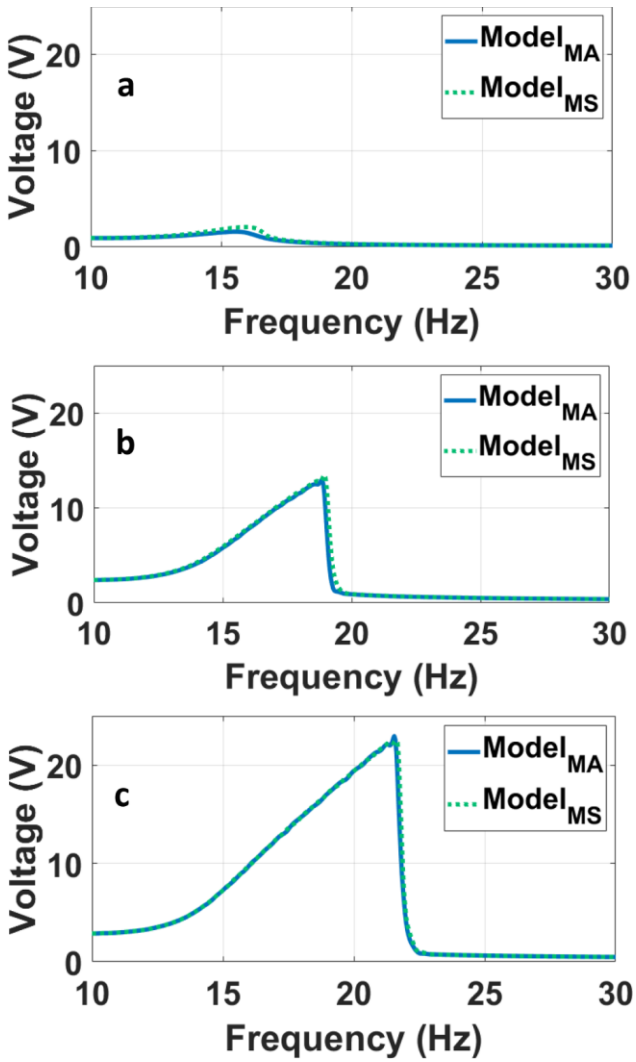

Figure 5-18: Close-circuit voltage frequency response obtained using model simulations at 1.25 g (m s2) across load resistors, R_l: (a) 100 Ω, (b) 1 kΩ , and (c) 10 kΩ. All model simulations are obtained using analytical force model (**Eq. 3-14**) in the equation of motion. However, $Model_{MA}$ uses analytical magnetic damping model (**Eq. 3-29**) in the equation of motion (**Eq. 3-1**), and $Model_{MS}$ uses the simplified magnetic damping model (**Eq. 3-30**) in the equation of motion (**Eq. 3-1**).

The results show that the dynamic model simulations generated using **Eq. 3-29** and **Eq. 3-30** coincide quite well. As a result, the commonly used method in the literature of incorporating a constant magnetic damping coefficient into the equation of motion to mimic the dynamic response of the vibration energy harvester gives a dependable

approximation. The greatest damping coefficient experienced by the harvester, i.e., C_m as shown in **Figure 5-17**, is used to determine the constant magnetic damping model.

In **Figure 5-19**, the influence of various design parameters found in **Eq. 3-29** on the magnetic damping induced in the energy harvester is explored. This is accomplished by altering the coil section's height, L, coil section's diameter, d, and coil section's axial position, ζ. Each of the previously indicated parameters was adjusted separately in these model simulations, while all other parameters in the magnetic damping force model were fixed at the nominal values stated in the table of nomenclature. The results show that when the coil section's height, L, diameter, d, or axial position, ζ, grows, the variance in the magnetic damping coefficient, C, diminishes; thus, the use of a constant damping coefficient, C_m, in **Eq. 3-30** is justifiable for a wide range of energy harvester dimensions.

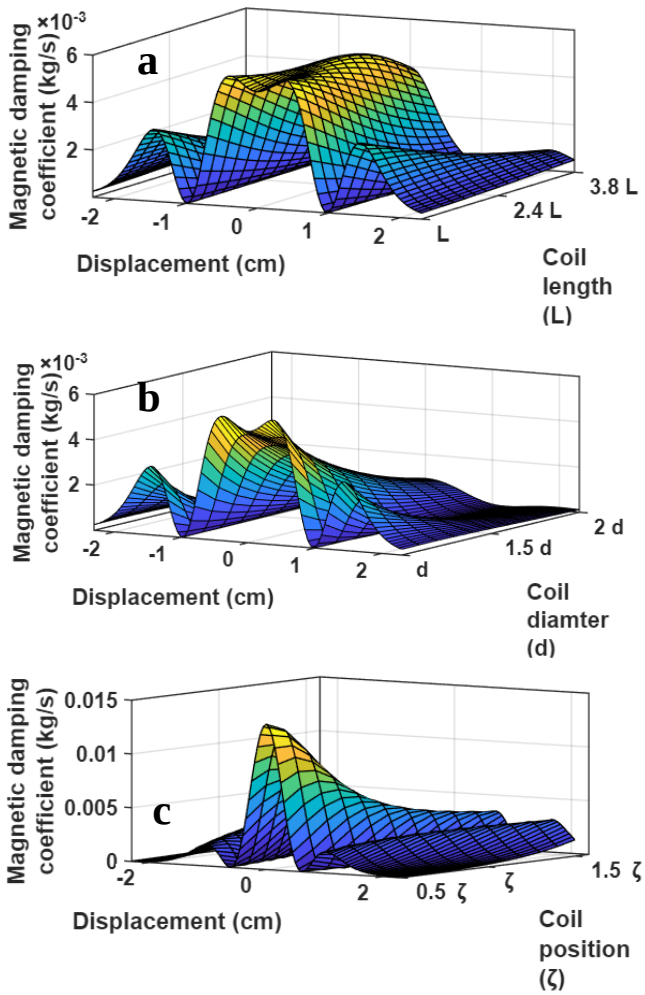

Figure 5-19: Magnetic damping coefficient, $C(z)$, with respect to the displacement, z, and the a) effect of coil length, L , b) effect of coil diameter, d , and c) effect of coil position, ζ . The load resistance in this simulation is$10\ k\Omega$.

5.2.3 Power Generation

The effects of design parameters on the power metrics of the magnetic spring-based vibration energy harvesting system are shown in **Figure 5-20**, **Figure 5-21**, **Figure 5-22**, **Figure 5-23**, **Figure 5-24**, and **Figure 5-25**. The volume of the levitated magnet (V), the remnant flux density of the levitated magnet ($B_{rf,lev}$), the height of stationary magnets (h), the inner diameter of stationary magnets (a), the outer diameter of stationary magnets (b), and the distance between the two stationary magnets (H) are all design

parameters. When running these model simulations, each of the previously specified parameters was modified separately, while the rest of the parameters in the dynamic model (**Eq. 3-1**) were kept at their nominal values from the nomenclature table. The results for the three load resistance values, R_{load} = 100 Ω, 1 kΩ, and 10 kΩ, are shown. The volume, (V), and remnant flux of the levitated magnet determine both the quantity of power generated by the energy harvester as well as the frequency peak location of the output power-frequency response envelop for a given load resistance, R_{load}. However, the other design parameters, such as the height of the stationary magnet (h), the inner diameter of stationary magnets (a), the outer diameter of stationary magnets (b), and the distance between the two stationary magnets (H), have a greater impact on the frequency peak location than on the harvester's output power.

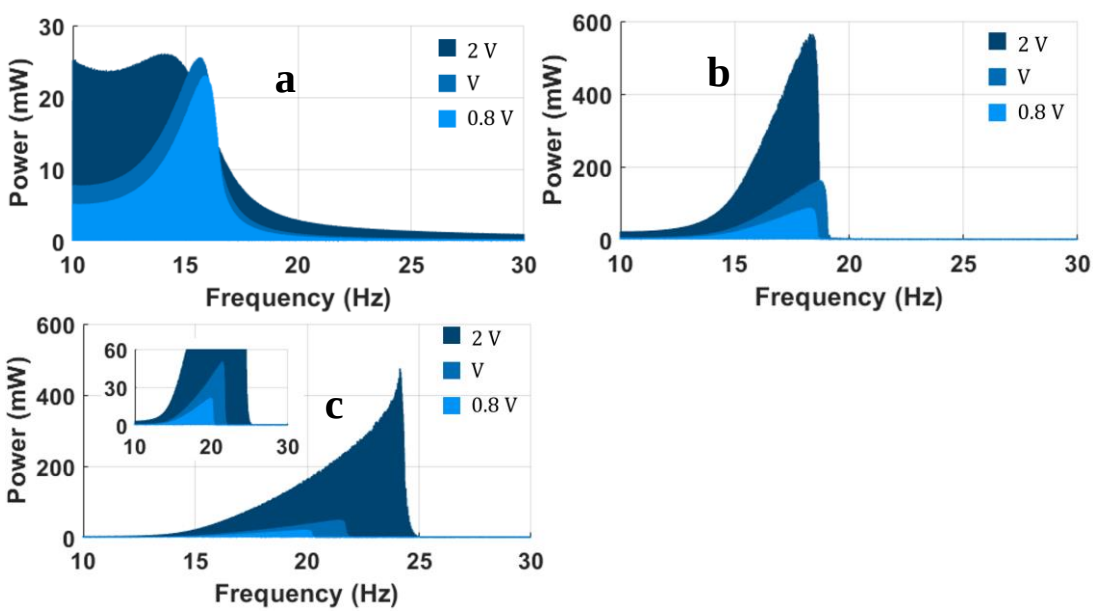

Figure 5-20: Effect of levitated magnet volume, V, on output power obtained using model simulations across various load resistors: a) R_{load} = 100 Ω, b) 1,000 Ω, and c) 10,000 Ω.

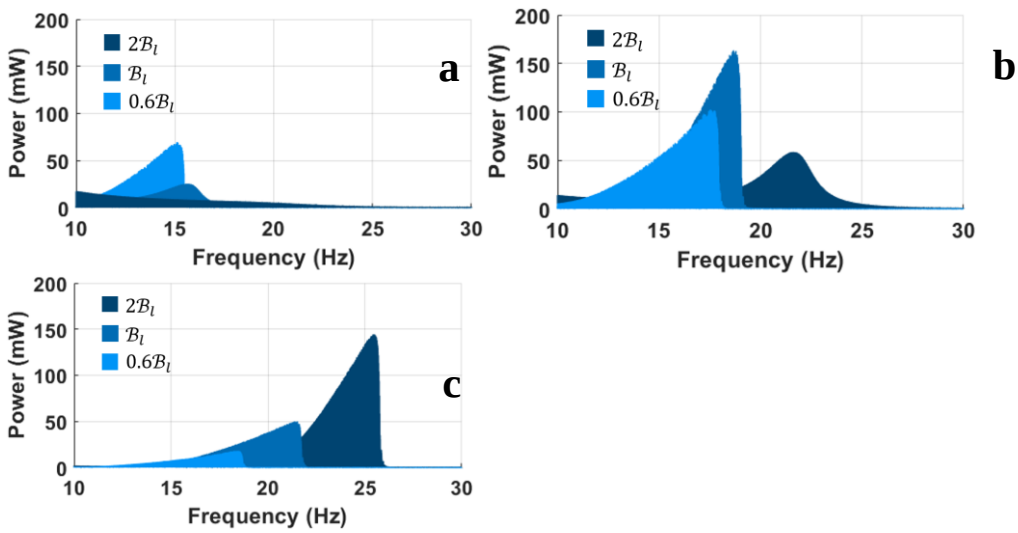

Figure 5-21: Effect of remnant magnetic flux density of the levitated magnet, $B_{rf,lev}$, on output power obtained using model simulations across various load resistors: a) $R_{load} = 100\ \Omega$, b) 1,000 Ω, and c) 10,000 Ω.

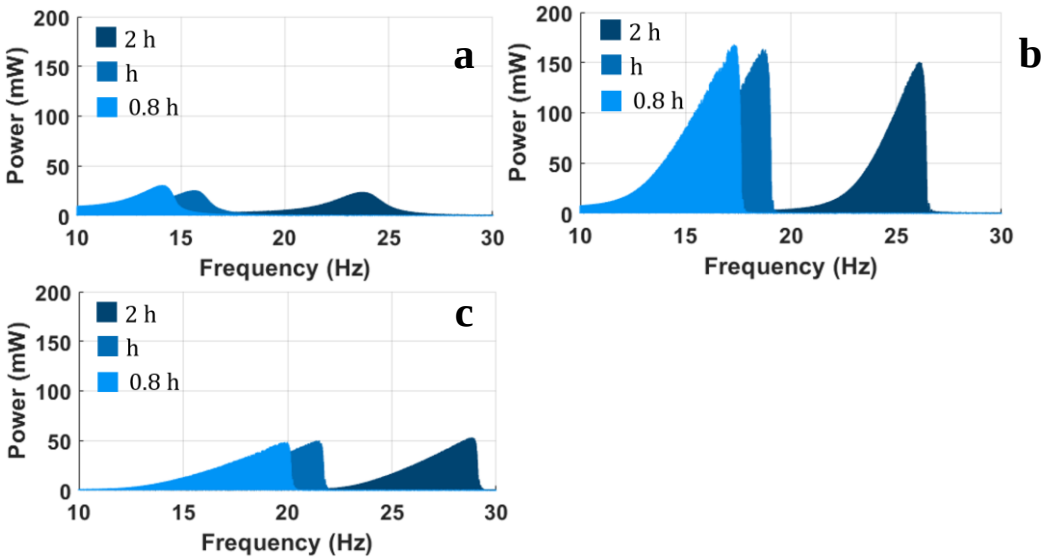

Figure 5-22: Effect of height of stationary magnets, (h), on output power obtained using model simulations across various load resistors: a) $R_l = 100\ \Omega$, b) 1,000 Ω, and c) 10,000 Ω.

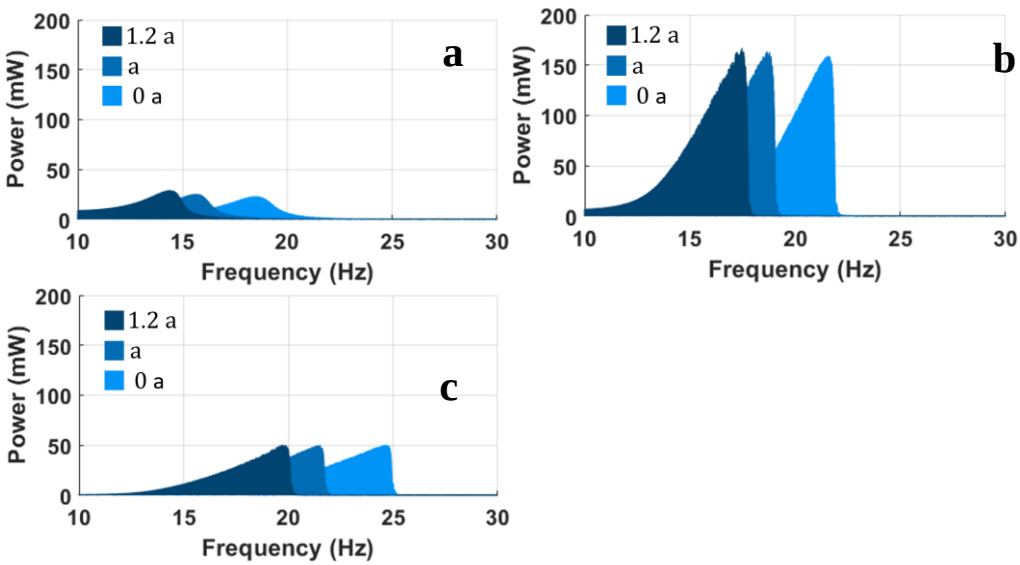

Figure 5-23: Effect of inner diameter of stationary magnets, (a), on output power obtained using model simulations across various load resistors: a) $R_{load} = 100\ \Omega$, b) 1,000 Ω, and c) 10,000 Ω.

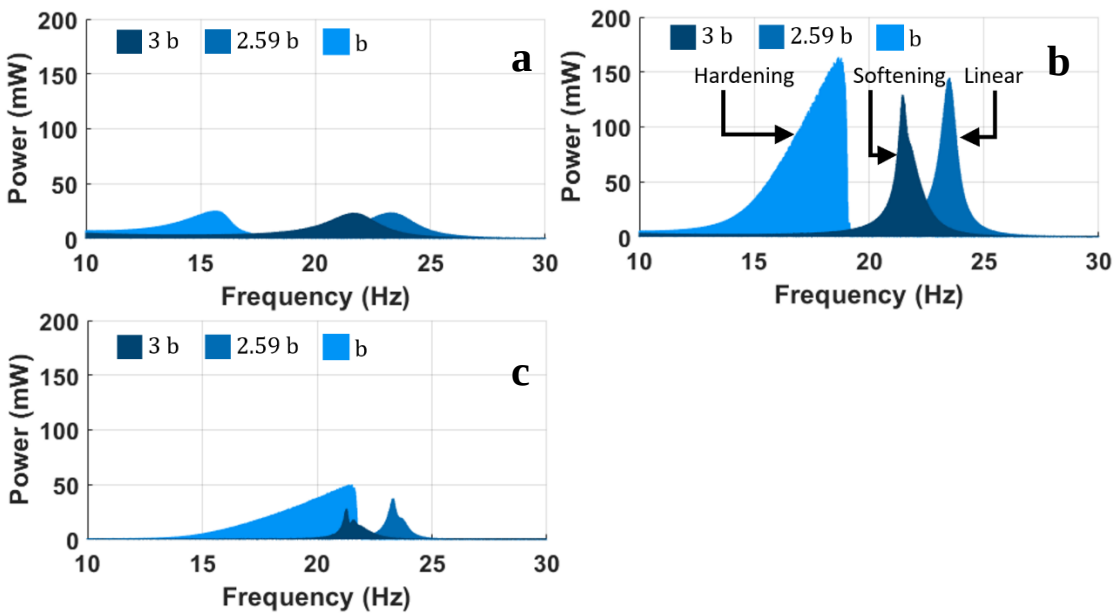

Figure 5-24: Effect of outer diameter of stationary magnets, (b), on output power obtained using model simulations across various load resistors: a) $R_{load} = 100\ \Omega$, b) 1,000 Ω, and c) 10,000 Ω.

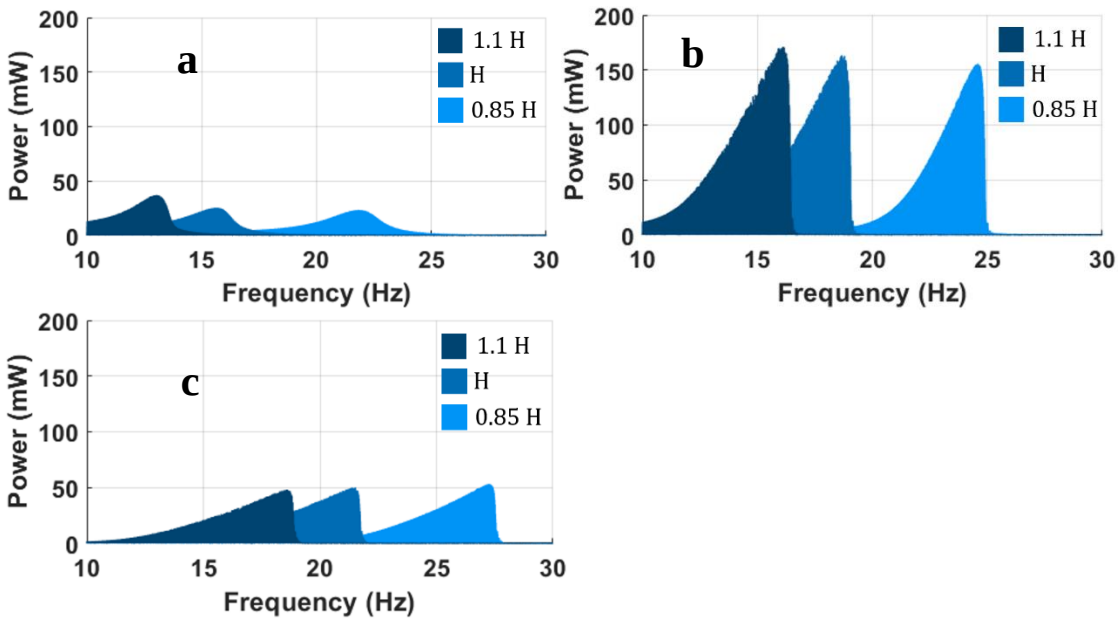

Figure 5-25: Effect of distance between the two stationary magnets, (H), on output power obtained using model simulations across various load resistors: a) $R_{load} = 100\ \Omega$, b) $1{,}000\ \Omega$, and c) $10{,}000\ \Omega$.

This is due to the fact that these design parameters (h, a, b, H) are related to stationary magnets and only affect the stiffness of the magnetic spring in the energy harvester for a particular load resistance. For example, as illustrated in **Figure 5-22**, raising the height of the stationary magnet, h, causes the frequency peak to shift to a higher value for fixed load resistance. In light of **Figure 5-16**, increasing the height of the stationary magnet, (h), results in a stiffer magnetic spring with larger stiffness coefficients, k_1 and k_3, thereby shifting the frequency jump to a higher value. Increasing the inner diameter of the stationary magnets, (a), **Figure 5-23**, and the distance between the two stationary magnets, (H), **Figure 5-25**, for a certain load resistance, R_{load}, changes the frequency jump to lower values due to the decrease in magnetic spring stiffness.

The influence of the stationary magnets' outer diameter, b, on the dynamic response of the vibration energy harvesting system follows. The linear, nonlinear

(hardening), and nonlinear (softening) frequency responses of the energy harvester may be seen at various values of the ring magnets' outer diameter, i.e., 2.59b, b, and 3b, respectively, when looking at **Figure 5-24**b (R_{load} = 1 kΩ).

In light of **Figure 5-24**b, this display of varied frequency responses occurring at various levels of b can be interpreted. The crucial value of the outer diameter, as shown in **Figure 5-24**, is b_c = 65 mm, which corresponds to roughly 2.59 b. The nonlinear stiffness coefficient, k_3, becomes zero, i.e., $k_3 = 0$, at this value of outer diameter, b, as illustrated in **Figure 5-16**d, while the linear stiffness coefficient, k_1, stays positive, resulting in a linear magnetic spring. As seen in **Figure 5-24**b, this phenomenon results in the energy harvester's linear dynamic behavior. When the outside diameter is less than the critical value, b = 25.4 mm, both the linear (k_1) and nonlinear (k_3) stiffness coefficients are positive, resulting in a hardening magnetic spring. The energy harvester's frequency response becomes nonlinear (hardening) as a result of this phenomenon. Finally, when the outer diameter, b, is somewhat more than the critical value, as shown in **Figure 5-16**d, the nonlinear stiffness coefficient, k_3, becomes negative while the linear stiffness coefficient, k_1, stays positive. The nonlinear (softening) dynamic behavior exhibited in **Figure 5-24**b is the result of this phenomenon.

Following that observation, the effect of the load resistance, R_{load}, is investigated. First, the results imply that changing the load resistance value, R_{load}, changes the frequency peak for a particular design parameter. This allows a given energy harvester's response to be tuned to a desired frequency range by simply changing the load resistance, R_{load}. For example, **Figure 5-22**a–c shows that at 100 Ω, 1 kΩ, and 10 kΩ, the frequency peak grew from 16 Hz to 19 Hz and subsequently 22 Hz for a fixed height of the

stationary magnet, h. Changes in magnetic dampening are most likely to blame for this shift in frequency jump. Nonetheless, the power generation suffers as a result of the frequency jump. As illustrated in **Figure 5-22**, as the load resistance, R_{load}, increases, the power generated by the harvester grows steadily until an optimum load resistance, R_{load} = 1 kΩ, is obtained. Any increase in load resistance above the optimum value results in a loss of power, as shown in **Figure 5-22**. The optimum load resistance, R_{load}, is also dependent on the remnant flux of the levitated magnet, $B_{rf,lev}$, as shown in **Figure 5-21**. At R_{load} = 1 kΩ, the power reaches its maximum value for the nominal value of the levitated magnet's remnant flux. When the remnant flux of the levitated magnet is increased to 2 $B_{rf,lev}$, however, the maximum power is achieved at an optimum load resistance of R_{load} = 10 kΩ. As demonstrated in **Eq. 3-29**, raising the remnant flux of the levitated magnet gives a greater magnetic damping force, resulting in a high optimum load resistance [63].

The findings of this study provide a foundation for designing and implementing magnetic springs in vibration energy harvesting devices. The utilization of these magnetic springs to scavenge freely accessible ambient vibrations around us opens up a lot of possibilities for giving electric power to gadgets and low-power sensors. Kim *et al*. used their electromagnetic vibration energy harvester to power wearable devices such as a timer and a pedometer, for example. With an average output of 7.68 mW and an optimal load resistance of 36, the harvester produced an open-circuit voltage of 1.39 V [13]. Pukar Maharjan *et al*. [14] developed an environmentally friendly wearable electromagnetic energy harvester for capturing vibrational energy from human body movements. With an ideal load resistance of around 104, the gadget produced 8.8 mW at

5 Hz. From 5 seconds of hand shaking, the energy harvester was used to run a stopwatch for approximately 16 minutes.

CHAPTER 6

CONCLUSIONS

This chapter concludes our work in mono-stability and bi-stability in magnetic spring based vibrational energy harvester. **Section 6.1** compares mono-stability and bi-stability. Specifically, **Section 6.1** points out the advantages and disadvantages in the vibration dynamic and electronic output of each mode. **Section 6.2** discusses in details the parametric study of mono-stability. **Section 6.2** summarizes our observations in modeling and approximating the behavior of mono-stability and discusses important highlights of how changing each design parameter can affect the behavior of the mono-stable device. The highlights of **Section 6.2** form a complete design guidelines for mono-stable magnetic spring based vibrational energy harvester. This chapter incorporates work from four publications by the author, previously published in November 2018 [20], November 2019 [21], February 2020 [22], and April 2020 [23]. It is reproduced here with the permission from all the coauthors involved in this study.

6.1 Monostable Vs. Bistable

Using experiment and model, a comparison of mono-stable and bi-stable magnetic-levitation-based vibration energy harvesters was carried out in this paper. Without the usage of extra piezoelectric devices, the selected design relies solely on magnetic contact. An oscillating magnet was levitated between two stationary top and bottom ring magnets in the mono-stable configuration. A bi-stable arrangement was

achieved by fixing a cluster of peripheral, solid magnets around the harvester shell. For power extraction, a coil was wrapped around the harvester's body. An energy harvester prototype was built, and its dynamic behavior under harmonic excitation was studied using an experiment and a model. Magnetic force models have been constructed analytically for both mono-stable and bi-stable setups. Model simulation results were in accurate agreement with measured force-displacement curves and those obtained with COMSOL software. These force models were then used to analyze the harvester's dynamic behavior by incorporating them into the equation of motion. The results of this comparison study showed that the analytical model of magnetic force offered more accurate results for the bi-stable configuration than the results obtained using the commonly utilized magnetic force polynomial fits. The results obtained using a polynomial fit of the magnetic force for the mono-stable configuration were in trustworthy agreement with the results obtained using experiment and the analytical force model. Furthermore, under harmonic excitation, mono-stability was found to be the more advantageous mode for vibration energy harvesting. According to the power measurements, the mono-stable design can provide more power at low acceleration than the bi-stable version can at high acceleration. Due to magnetic dampening, the optimum load resistance of the mono-stable configuration was higher than that of the bi-stable design, according to the power measurements. The bi-stable architecture benefits from thinner peripheral magnets, especially at lower acceleration values. Lower energy barriers, improved frequency responses, and nearly zero stiffness near the equilibrium position were all achieved using thinner peripheral magnets. The harvester's mono-stability was caused by the employment of thinner peripheral magnets.

6.2 Design of Magnetic Springs

We have seen remarkable breakthroughs in the field of wearable smart electronics and sensors in recent years. These remarkable technological breakthroughs have created a pressing demand for portable power sources that can take use of freely available energy sources such as ambient vibrations. Vibrations generated by human body motion, dynamic structures, and machinery are among the many structures and items that emit these numerous and free vibrations. The ability of a vibration energy harvesting device to transform kinetic energy from ambient vibrations into useable electric power is its essence. Magnetic spring-based vibration energy harvesting systems have exploded in popularity in recent years as a result of this.

Design guidelines and the effects of various design parameters of magnetic springs used in vibration energy harvesting systems are investigated in this article, assisting designers in understanding and investigating the dynamic response and performance of energy harvesting systems in light of their design parameters, such as geometry, dimensions, and material properties. Experimental data is used to validate the constructed theoretical framework, which exhibits excellent agreement. In addition, this paper derives and presents approximate analytical equations for linear and nonlinear stiffness coefficients. The current study's findings revealed the following:

• The magnetic damping coefficient of the energy harvesting system varies during dynamic operation and is dependent on the position of the levitated magnet during harvester operation. Nonetheless, the usual method of estimating the magnetic damping

coefficient as a constant yields accurate predictions of the energy harvesting system's dynamic behavior.

• At low acceleration levels, the traditional technique of representing the nonlinear magnetic force with a polynomial function and then implementing the polynomial force function into the equation of motion of the energy harvesting system provides adequate results that are comparable to measured data. The use of a polynomial function to describe the nonlinear magnetic force in the harvester's equation of motion will most likely result in an underestimation of the energy harvesting system's dynamic response at high acceleration levels. The energy harvesting system's dynamic response may be predicted accurately at greater acceleration levels by incorporating an analytical model of the magnetic spring force into the equation of motion.

• The volume of the levitated magnet, the height of stationary magnets, the inner diameter of stationary magnets, the outer diameter of stationary magnets, and the distance between the two stationary magnets are all design parameters that influence the linear and nonlinear stiffness coefficients of the magnetic spring. The linear and nonlinear stiffness coefficients are related to the volume of the levitated magnet and the height of the stationary magnets, and inversely proportional to the stationary magnets' inner diameter and the distance between them.

• The linear and nonlinear stiffness coefficients, and thus the dynamic behavior of the vibration energy harvesting system, are greatly influenced by the outer diameter of the stationary ring magnets in the magnetic spring configuration. By carefully selecting the right outer diameter for the stationary ring magnet, the magnetic spring-based vibration energy harvesting system can be transformed into a linear, hardening nonlinear,

or softening nonlinear dynamic system. A linear energy harvesting system results from a crucial value of the ring magnet's outer diameter, whereas reducing the outer diameter beyond this critical value results in a hardening nonlinear vibration energy harvesting system. When the outer diameter increases beyond the critical value, the nonlinear vibration energy harvesting system softens.

• The volume and remnant flux of the levitated magnet affect both the amount of power generated and the location of the frequency jump for a fixed load resistance. However, the height of stationary magnets, the inner diameter of stationary magnets, the outer diameter of stationary magnets, and the distance between the two stationary magnets mainly affect the frequency jump location rather than the amount of output power generated by the harvester.

• To get a desired frequency range, the load resistance can be employed to modify the dynamic response of the magnetic spring-based vibration energy harvesting system. The change in magnetic damping causes the frequency jump to shift. Regardless, this frequency shift comes at the expense of electricity generation. As the load resistance grows, the power supplied by the harvester increases, and the frequency leap shifts steadily until an ideal load resistance is obtained. Increases in load resistance beyond the optimum value cause a change in the frequency jump, as well as a decline in output power.

• In a magnetic spring-based vibration energy harvesting system, the remnant flux of the levitated magnet is a critical design parameter that can affect the optimum load resistance value. The magnetic damping force changes when the remnant-flux of the levitated magnet changes. This affects the optimum load resistance.

The research described in this paper paves the way for more research into magnetic springs, which are extensively employed in energy systems. That is, the growing interest in using magnetic springs in a variety of energy systems and applications positions the presented work as a tool and platform for the design and analysis of a variety of magnetic spring-based energy systems, including vibration energy harvesting systems and energy sinks.

APPENDIX

NOMENCLATURE

Symbol	Definition	Value	Unit
a	The inner radius of a ring magnet	6.35	mm
A	Acceleration of excitation source	-	$m\ s^{-2}$
b	The outer radius of a ring magnet	12.7	mm
B	The magnetic field along the z axis of the stationary top and bottom ring magnets	-	T
B_{coil}	The magnetic field generated by current in a coil	-	T
B_{cyl}	The magnetic field along the z axis of a cylindrical magnet	-	T
B_i	The magnetic field along the z axis of generated by the induced current in a single coil turn	-	T
$B_{rf,lev}$	Residual flux density of the levitated magnet	1.48	T
$B_{rf,ring}$	Residual flux density of a ring magnet	-1.32	T
B_z	The magnetic field along the z axis of a levitated magnet	-	T
c	Damping coefficient due to structural and aerodynamic energy losses	-	$kg\ s^{-1}$
C	Magnetic damping coefficient, a function of the levitated magnet's relative position z	-	$kg\ s^{-1}$
F_{bot}	Magnetic force acting on the levitated magnet from the stationary bottom ring magnet	-	N
F_{cyl}	Magnetic force acting on the levitated magnet from a peripheral magnet	-	N
F_{damp}	Total damping force acting on the levitated magnet	-	N
F_e	Damping force acting on the levitated magnet due to the induced current in a coil	-	N
F_{e_1}	Damping force acting on the levitated magnet due to the induced current in the top coil	-	N
F_{e_2}	Damping force acting on the levitated magnet due to the induced current in the bottom coil	-	N
F_{eddy}	Damping force acting on the levitated magnet due to the induced current in the surrounding coil	-	N
F_g	Gravitational force acting on the levitated magnet	-	N
F_i	The magnetic damping force from the induced current in a coil turn acting on the levitated magnet		

F_{mag}	Total magnetic force acting on the levitated magnet	-	N
F_{ring}	Magnetic force acting on the levitated magnet from a stationary ring magnet	-	N
F_{top}	Magnetic force acting on the levitated magnet from the stationary top ring magnet	-	N
g	Gravitational acceleration	9.81	$m\ s^{-2}$
h	Height of the stationary ring magnets	12.7	mm
H	The distance between the two stationary ring magnets	-	m
i	The index of a single coil turn	-	1
I	Induced current in a coil turn	-	A
k_1	The linear term in the polynomial approximation of the magnetic force	-	N/m
k_3	The nonlinear term in the polynomial approximation of the magnetic force	-	N/m
L	Half the length of a coil	-	m
m	Mass of the levitated magnet	14.017	g
m_{cyl}	Magnetic dipole moment of each cylindrical magnet of the cluster of middle (peripheral) magnets.	16.635	$mA\ m^2$
m_{lev}	Magnetic dipole moment of the levitated magnet	1.68992	$A\ m^2$
M	The magnetization of a stationary ring magnet	-1,050	$A\ mm^{-1}$
$\vec{M}$	The magnetization vector of a stationary ring magnet		
$\vec{M}_{bot}$	The magnetization of the stationary bottom ring magnet	-1,050	$A\ mm^{-1}$
$\vec{M}_{top}$	The magnetization of the stationary top ring magnet	-1,050	$A\ mm^{-1}$
n	Number of middle (peripheral) magnets in one layer	10	1
N	Number of stable positions	-	1
N_c	Number of coil turns in top or bottom coil section	500	1
P	Predicted power		
$\vec{r}$	The vector position of the point of magnetic field evaluation	-	m
$\vec{r'}$	The vector position of a dipole	-	m
R_{coil}	Resistance of the coil	193	Ω
R_{load}	Resistance of the load	193	Ω
$\vec{s}$	Vector normal to the top and the bottom surfaces of a ring magnet	-	m^2
t	Time	-	s
U	The potential energy of the levitated magnet	-	J
V	Volume of the levitated magnet	1.609	cm^3
x	The absolute position of the levitated magnet	-	m
$\dot{x}$	The absolute velocity of the levitated magnet	-	$m\ s^{-1}$
$\ddot{x}$	The absolute acceleration of the levitated magnet	-	$m\ s^{-2}$
y	Axial position of the shaker table	-	m
$\dot{y}$	Velocity of the shaker table		
z	The relative position of the levitated magnet	-	m
$\hat{z}$	Unit vector of the z-axis	1	1

$\dot{z}$	The relative velocity of the levitated magnet	-	$m\ s^{-1}$
$\ddot{z}$	The relative acceleration of the levitated magnet	-	$m\ s^{-2}$
z_b	Position of the stationary bottom magnet	-43.18	mm
z_c	Axial position of a single coil turn	-	m
z_{cb}	Axial position of the center of the bottom coil	-9.5	mm
z_{coil}	Axial position of the center of a coil	-	m
z_{ct}	Axial position of the center of the top coil	9.5	mm
z_{cyl}	The axial position of a fixed middle (peripheral) magnet	-	m
z_i	Position of a single coil turn	-	m
z_r	The axial position of a ring magnet	-	m
z_s	An axial position		
z_t	Position of the stationary top fixed magnet	43.18	mm
$\mathcal{E}$	Electromotive force in all coil turns	-	V
$\mathcal{E}_1$	Electromotive force in the top coil section	-	V
$\mathcal{E}_2$	Electromotive force in the bottom coil section	-	V
$\mathcal{E}_c$	Electromotive force in a coil	-	V
$\mathcal{E}_m$	The measured voltage in a closed circuit test		
ϕ	Magnetic flux in a coil	-	Wb
ϕ_i	Magnetic flux in a single coil turn	-	Wb
μ_0	Permeability of free space	$4\pi \times 10^{-7}$	$H\ m^{-1}$
ρ	A general radial position in cylindrical coordinate system	-	m
ρ_{coil}	The average radius of the coil	8.77	mm
ρ_{mid}	The distance between the center of each middle (peripheral) magnet and the z axis	13.49	mm
ψ	The scalar magnetic potential	-	A
ω	Driving frequency	-	$rad\ s^{-1}$

BIBLIOGRAPHY

[1] S. Patel, H. Park, P. Bonato, L. Chan, and M. Rodgers, "A review of wearable sensors and systems with application in rehabilitation," *J. Neuroeng. Rehabil.*, vol. 9, no. 1, p. 21, 2012, doi: 10.1186/1743-0003-9-21.

[2] C. Knight, J. Davidson, and S. Behrens, "Energy Options for Wireless Sensor Nodes," *Sensors (Basel).*, vol. 8, no. 12, pp. 8037–8066, Dec. 2008, doi: 10.3390/s8128037.

[3] M. P. Soares Dos Santos *et al.*, "New cosurface capacitive stimulators for the development of active osseointegrative implantable devices," *Sci. Rep.*, vol. 6, p. 30231, Jul. 2016, doi: 10.1038/srep30231.

[4] M. P. Soares dos Santos, J. A. F. Ferreira, A. Ramos, and J. A. O. Simões, "Active orthopaedic implants: Towards optimality," *J. Franklin Inst.*, vol. 352, no. 3, pp. 813–834, 2015, doi: https://doi.org/10.1016/j.jfranklin.2014.11.005.

[5] N. Silva *et al.*, "Power management architecture for smart hip prostheses comprising multiple energy harvesting systems," *Sensors Actuators, A Phys.*, vol. 202, pp. 183–192, Nov. 2013, doi: 10.1016/j.sna.2013.01.049.

[6] M. Amin Karami and D. J. Inman, "Powering pacemakers from heartbeat vibrations using linear and nonlinear energy harvesters," *Appl. Phys. Lett.*, vol. 100, no. 4, p. 42901, Jan. 2012, doi: 10.1063/1.3679102.

[7] G. J. Renzenbrink and M. J. Ijzerman, "Percutaneous neuromuscular electrical stimulation (P-NMES) for treating shoulder pain in chronic hemiplegia. Effects on shoulder pain and quality of life," *Clin. Rehabil.*, vol. 18, no. 4, pp. 359–365, Jun. 2004, doi: 10.1191/0269215504cr759oa.

[8] N. Elvin, N. Lajnef, and A. Elvin, "Feasibility of Structural Monitoring With Vibration Powered Sensors," *Smart Mater. Struct.*, vol. 15, p. 977, Jun. 2006, doi: 10.1088/0964-1726/15/4/011.

[9] P. Constantinou and S. Roy, "A non-linear 3D printed electromagnetic vibration energy harvester," *J. Phys. Conf. Ser.*, vol. 660, p. 12092, Dec. 2015, doi: 10.1088/1742-6596/660/1/012092.

[10] S. J. Roundy. "Energy scavenging for wireless sensor nodes with a focus on vibration to electricity conversion," *PhD Dissertation*, Berkeley 2003. [Available from ProQuest Dissertations & Theses A&I; ProQuest Dissertations & Theses Global. (305340201).].

[11] S. Priya and D. J. Inman, *Energy Harvesting Technologies*. Springer US, 2008.

[12] N. Elvin, *Advances in Energy Harvesting Methods*. 2013.

[13] J. W. Kim, M. Salauddin, H. Cho, M. S. Rasel, and J. Y. Park, "Electromagnetic energy harvester based on a finger trigger rotational gear module and an array of disc Halbach magnets," *Appl. Energy*, vol. 250, pp. 776–785, 2019, doi: https://doi.org/10.1016/j.apenergy.2019.05.059.

[14] P. Maharjan, T. Bhatta, M. S. Rasel, M. Salauddin, M. T. Rahman, and J. Y. Park, "High-performance cycloid inspired wearable electromagnetic energy harvester for scavenging human motion energy," *Appl. Energy*, vol. 256, p. 113987, 2019.

[15] S. Ju and C.-H. Ji, "Impact-based piezoelectric vibration energy harvester," *Appl. Energy*, vol. 214, pp. 139–151, 2018, doi: https://doi.org/10.1016/j.apenergy.2018.01.076.

[16] G. Aldawood, H. T. Nguyen, and H. Bardaweel, "Improving Power and Frequency Bandwidth of a Magnetic Spring Based Vibration Energy Harvester Using FR4 Spring-Guided Magnet." in *ASME International Mechanical Engineering Congress and Exposition* (Vol. 59414, p. V004T05A107). American Society of Mechanical Engineers. Nov. 11, 2019, doi: 10.1115/IMECE2019-10174.

[17] G. Aldawood, H. Nguyen, and H. Bardaweel, "High power density spring-assisted nonlinear electromagnetic vibration energy harvester for low base-accelerations," *Appl. Energy*, vol. 253, no. June, p. 113546, 2019, doi: 10.1016/j.apenergy.2019.113546.

[18] P. Carneiro *et al.*, "Electromagnetic energy harvesting using magnetic levitation architectures: A review," *Applied Energy*. 2020, doi: 10.1016/j.apenergy.2019.114191.

[19] J. Conti, P. Holtberg, J. Diefenderfer, A. LaRose, J. T. Turnure, and L. Westfall, "International Energy Outlook 2016 With Projections to 2040," *US Department of Energy Report* No. DOE/EIA-0484(2016), doi: 10.2172/1296780.

[20] H. Nguyen and H. Bardaweel, "Multi-Stable Magnetic Spring-Based Energy Harvester Subject to Harmonic Excitation: Comparative Study and Experimental Evaluation." in *ASME International Mechanical Engineering Congress and Exposition* (Vol. 52040, p. V04BT06A038). American Society of Mechanical Engineers. Nov. 09, 2018, doi: 10.1115/IMECE2018-86157.

[21] H. Nguyen, D. Genov, and H. Bardaweel, “Mono-stable and bi-stable magnetic spring based vibration energy harvesting systems subject to harmonic excitation: Dynamic modeling and experimental verification,” *Mech. Syst. Signal Process.*, vol. 134, p. 106361, 2019, doi: 10.1016/j.ymssp.2019.106361.

[22] H. Nguyen, D. A. Genov, and H. Bardaweel, “Vibration energy harvesting using magnetic spring based nonlinear oscillators: Design strategies and insights,” *Appl. Energy*, vol. 269, no. February, p. 115102, 2020, doi: 10.1016/j.apenergy.2020.115102.

[23] H. T. Nguyen and H. Bardaweel, “Design guidelines and parametric study of nonlinear magnetic springs for vibration systems,” in *Proc.SPIE*, Apr. 2020, vol. 11387, doi: 10.1117/12.2556129.

[24] D. J. Apo and S. Priya, “High Power Density Levitation-Induced Vibration Energy Harvester,” *Energy Harvest. Syst.*, 2014, doi: 10.1515/ehs-2013-0005.

[25] D. F. Berdy, D. J. Valentino, and D. Peroulis, “Design and optimization of a magnetically sprung block magnet vibration energy harvester,” *Sensors Actuators A Phys.*, vol. 218, pp. 69–79, 2014, doi: https://doi.org/10.1016/j.sna.2014.06.011.

[26] M. P. Soares dos Santos *et al.*, “Magnetic levitation-based electromagnetic energy harvesting: a semi-analytical non-linear model for energy transduction,” *Sci. Rep.*, vol. 6, no. 1, p. 18579, 2016, doi: 10.1038/srep18579.

[27] B. P. Mann and N. D. Sims, “Energy harvesting from the nonlinear oscillations of magnetic levitation,” *J. Sound Vib.*, 2009, doi: 10.1016/j.jsv.2008.06.011.

[28] Q. Zhang, Y. Wang, and E. S. Kim, “Electromagnetic Energy Harvester With Flexible Coils and Magnetic Spring for 1–10 Hz Resonance,” *J. Microelectromechanical Syst.*, vol. 24, no. 4, pp. 1193–1206, 2015, doi: 10.1109/JMEMS.2015.2393911.

[29] C. Lee, D. Stamp, N. R. Kapania, and J. O. Mur-Miranda, “Harvesting vibration energy using nonlinear oscillations of an electromagnetic inductor,” in *Energy harvesting and storage: Materials, Devices, and Applications* (Vol. 7683, pp. 162-173). SPIE. 2010, doi: 10.1117/12.849895.

[30] D. Mallick, A. Amann, and S. Roy, “A nonlinear stretching based electromagnetic energy harvester on FR4 for wideband operation,” *Smart Mater. Struct.*, vol. 24, no. 1, p. 15013, 2014, doi: 10.1088/0964-1726/24/1/015013.

[31] R. Ramlan, M. J. Brennan, I. Kovacic, B. R. Mace, and S. G. Burrow, “Exploiting knowledge of jump-up and jump-down frequencies to determine the parameters of a Duffing oscillator,” *Commun. Nonlinear Sci. Numer. Simul.*, vol. 37, pp. 282–291, 2016, doi: https://doi.org/10.1016/j.cnsns.2016.01.017.

[32] P. L. Green, K. Worden, K. Atallah, and N. D. Sims, “The effect of Duffing-type non-linearities and Coulomb damping on the response of an energy harvester to random excitations,” *J. Intell. Mater. Syst. Struct.*, vol. 23, no. 18, pp. 2039–2054, May 2012, doi: 10.1177/1045389X12446520.

[33] P. ~L. Green, K. Worden, and N. ~D. Sims, “On the identification and modelling of friction in a randomly excited energy harvester,” *J. Sound Vib.*, vol. 332, no. 19, pp. 4696–4708, Sep. 2013, doi: 10.1016/j.jsv.2013.04.024.

[34] I. Abed, N. Kacem, M. L. Bouazizi, and N. Bouhaddi, “Nonlinear 2-DOFs Vibration Energy Harvester Based on Magnetic Levitation BT - Shock & Vibration, Aircraft/Aerospace, and Energy Harvesting, Volume 9,” 2015, pp. 39–45.

[35] Y. Zhang, C. S. Cai, and B. Kong, “A low frequency nonlinear energy harvester with large bandwidth utilizing magnet levitation,” *Smart Mater. Struct.*, vol. 24, p. 45019, Apr. 2015, doi: 10.1088/0964-1726/24/4/045019.

[36] M. Gutierrez, A. Shahidi, D. Berdy, and D. Peroulis, “Design and characterization of a low frequency 2-dimensional magnetic levitation kinetic energy harvester,” *Sensors Actuators A Phys.*, vol. 236, pp. 1–10, 2015, doi: https://doi.org/10.1016/j.sna.2015.10.009.

[37] S. Palagummi and F. G. Yuan, “An optimal design of a mono-stable vertical diamagnetic levitation based electromagnetic vibration energy harvester,” *J. Sound Vib.*, vol. 342, pp. 330–345, Apr. 2015, doi: 10.1016/j.jsv.2014.12.034.

[38] X. Yang, B. Zhang, J. Li, and Y. Wang, “Model and Experimental Research on an Electromagnetic Vibration-Powered Generator With Annular Permanent Magnet Spring,” *IEEE Trans. Appl. Supercond.*, vol. 22, no. 3, p. 5201504, 2012, doi: 10.1109/TASC.2011.2179401.

[39] R. L. Harne and K. W. Wang, “A review of the recent research on vibration energy harvesting via bistable systems,” *Smart Mater. Struct.*, vol. 22, no. 2, p. 23001, 2013, doi: 10.1088/0964-1726/22/2/023001.

[40] G. Wang, W.-H. Liao, B. Yang, X. Wang, W. Xu, and X. Li, “Dynamic and energetic characteristics of a bistable piezoelectric vibration energy harvester with an elastic magnifier,” *Mech. Syst. Signal Process.*, vol. 105, pp. 427–446, 2018, doi: https://doi.org/10.1016/j.ymssp.2017.12.025.

[41] M. Ferrari, V. Ferrari, M. Guizzetti, B. Andò, S. Baglio, and C. Trigona, “Improved energy harvesting from wideband vibrations by nonlinear piezoelectric converters,” *Sensors Actuators A Phys.*, vol. 162, no. 2, pp. 425–431, 2010, doi: https://doi.org/10.1016/j.sna.2010.05.022.

[42] M. F. Daqaq, R. Masana, A. Erturk, and D. Dane Quinn, “On the Role of Nonlinearities in Vibratory Energy Harvesting: A Critical Review and Discussion,” *Appl. Mech. Rev.*, vol. 66, no. 4, May 2014, doi: 10.1115/1.4026278.

[43] C. Lan and W. Qin, “Enhancing ability of harvesting energy from random vibration by decreasing the potential barrier of bistable harvester,” *Mech. Syst. Signal Process.*, vol. 85, pp. 71–81, 2017, doi: https://doi.org/10.1016/j.ymssp.2016.07.047.

[44] Z. Yang, S. Zhou, J. Zu, and D. Inman, “High-Performance Piezoelectric Energy Harvesters and Their Applications,” *Joule*, vol. 2, no. 4, pp. 642–697, 2018, doi: https://doi.org/10.1016/j.joule.2018.03.011.

[45] S. Zhou, J. Cao, D. J. Inman, J. Lin, S. Liu, and Z. Wang, “Broadband tristable energy harvester: Modeling and experiment verification,” *Appl. Energy*, vol. 133, pp. 33–39, 2014, doi: https://doi.org/10.1016/j.apenergy.2014.07.077.

[46] J. Cao, S. Zhou, W. Wang, and J. Lin, “Influence of potential well depth on nonlinear tristable energy harvesting,” *Appl. Phys. Lett.*, vol. 106, no. 17, p. 173903, Apr. 2015, doi: 10.1063/1.4919532.

[47] J. Zhou, K. Wang, D. Xu, and H. Ouyang, “Local resonator with high-static-low-dynamic stiffness for lowering band gaps of flexural wave in beams,” *J. Appl. Phys.*, vol. 121, no. 4, p. 44902, Jan. 2017, doi: 10.1063/1.4974299.

[48] Z. Zhou, W. Qin, and P. Zhu, “Improve efficiency of harvesting random energy by snap-through in a quad-stable harvester,” *Sensors Actuators A Phys.*, vol. 243, pp. 151–158, 2016, doi: https://doi.org/10.1016/j.sna.2016.03.024.

[49] Z. Zhou, W. Qin, and P. Zhu, “Harvesting performance of quad-stable piezoelectric energy harvester: Modeling and experiment,” *Mech. Syst. Signal Process.*, vol. 110, pp. 260–272, 2018, doi: https://doi.org/10.1016/j.ymssp.2018.03.023.

[50] B. P. Mann and B. A. Owens, “Investigations of a nonlinear energy harvester with a bistable potential well,” *J. Sound Vib.*, vol. 329, no. 9, pp. 1215–1226, 2010, doi: https://doi.org/10.1016/j.jsv.2009.11.034.

[51] A. Erturk and D. J. Inman, “Broadband piezoelectric power generation on high-energy orbits of the bistable Duffing oscillator with electromechanical coupling,” *J. Sound Vib.*, vol. 330, no. 10, pp. 2339–2353, 2011, doi: https://doi.org/10.1016/j.jsv.2010.11.018.

[52] Ö. Zorlu, E. T. Topal, and H. Külah, “A Vibration-Based Electromagnetic Energy Harvester Using Mechanical Frequency Up-Conversion Method,” *IEEE Sens. J.*, vol. 11, no. 2, pp. 481–488, 2011, doi: 10.1109/JSEN.2010.2059007.

[53] M. Liu *et al.*, “Design, simulation and experiment of a novel high efficiency energy harvesting paver,” *Appl. Energy*, vol. 212, pp. 966–975, 2018, doi: https://doi.org/10.1016/j.apenergy.2017.12.123.

[54] Z. Zhang *et al.*, “A high-efficiency energy regenerative shock absorber using supercapacitors for renewable energy applications in range extended electric vehicle,” *Appl. Energy*, vol. 178, pp. 177–188, 2016, doi: https://doi.org/10.1016/j.apenergy.2016.06.054.

[55] Z. Zhou, W. Qin, and P. Zhu, “A broadband quad-stable energy harvester and its advantages over bi-stable harvester: Simulation and experiment verification,” *Mech. Syst. Signal Process.*, vol. 84, pp. 158–168, 2017, doi: https://doi.org/10.1016/j.ymssp.2016.07.001.

[56] D. J. Griffiths, *Introduction to electrodynamics*. 2017. Cambridge University Press, London.

[57] P. Podder, P. Constantinou, D. Mallick, A. Amann, and S. Roy, “Magnetic Tuning of Nonlinear MEMS Electromagnetic Vibration Energy Harvester,” *J. Microelectromechanical Syst.*, vol. 26, no. 3, pp. 539–549, 2017, doi: 10.1109/JMEMS.2017.2672638.

[58] M. J. (Michael J. Brennan and I. Kovacic, *The Duffing equation nonlinear oscillators and their behaviour* . Chichester, West Sussex: Wiley, 2011.

[59] R. Ramlan, M. J. Brennan, B. R. Mace, and I. Kovacic, “Potential benefits of a non-linear stiffness in an energy harvesting device,” *Nonlinear Dyn.*, vol. 59, no. 4, pp. 545–558, 2010, doi: 10.1007/s11071-009-9561-5.

[60] G. Dong, X. Zhang, S. Xie, B. Yan, and Y. Luo, “Simulated and experimental studies on a high-static-low-dynamic stiffness isolator using magnetic negative stiffness spring,” *Mech. Syst. Signal Process.*, vol. 86, pp. 188–203, 2017.

[61] S. Dhote, Z. Yang, K. Behdinan, and J. Zu, “Enhanced broadband multi-mode compliant orthoplanar spring piezoelectric vibration energy harvester using magnetic force,” *Int. J. Mech. Sci.*, vol. 135, pp. 63–71, 2018.

[62] J. Bian and X. Jing, “Superior nonlinear passive damping characteristics of the bio-inspired limb-like or X-shaped structure,” *Mech. Syst. Signal Process.*, vol. 125, pp. 21–51, 2019, doi: https://doi.org/10.1016/j.ymssp.2018.02.014.

[63] M. Ghandchi Tehrani and S. J. Elliott, “Extending the dynamic range of an energy harvester using nonlinear damping,” *J. Sound Vib.*, vol. 333, no. 3, pp. 623–629, 2014, doi: https://doi.org/10.1016/j.jsv.2013.09.035.